

University of New Hampshire
University of New Hampshire Scholars' Repository

Master's Theses and Capstones

Student Scholarship

Fall 2008

Satellite-based auroral tomography and time-varying volume reconstruction

Hyojin Kim

University of New Hampshire, Durham

Follow this and additional works at: <https://scholars.unh.edu/thesis>

Recommended Citation

Kim, Hyojin, "Satellite-based auroral tomography and time-varying volume reconstruction" (2008). *Master's Theses and Capstones*. 387. <https://scholars.unh.edu/thesis/387>

This Thesis is brought to you for free and open access by the Student Scholarship at University of New Hampshire Scholars' Repository. It has been accepted for inclusion in Master's Theses and Capstones by an authorized administrator of University of New Hampshire Scholars' Repository. For more information, please contact nicole.hentz@unh.edu.

**SATELLITE-BASED AURORAL TOMOGRAPHY AND
TIME-VARYING VOLUME RECONSTRUCTION**

BY

HYOJIN KIM

B.S. in Systems Management Engineering, Sungkyunkwan University, S. Korea, 2001

THESIS

Submitted to the University of New Hampshire

In Partial Fulfillment of

The Requirements for the Degree of

Master of Science

In

Computer Science

September, 2008

UMI Number: 1459502

INFORMATION TO USERS

The quality of this reproduction is dependent upon the quality of the copy submitted. Broken or indistinct print, colored or poor quality illustrations and photographs, print bleed-through, substandard margins, and improper alignment can adversely affect reproduction.

In the unlikely event that the author did not send a complete manuscript and there are missing pages, these will be noted. Also, if unauthorized copyright material had to be removed, a note will indicate the deletion.

UMI[®]

UMI Microform 1459502

Copyright 2008 by ProQuest LLC.

All rights reserved. This microform edition is protected against unauthorized copying under Title 17, United States Code.

ProQuest LLC
789 E. Eisenhower Parkway
PO Box 1346
Ann Arbor, MI 48106-1346

This thesis has been examined and approved.



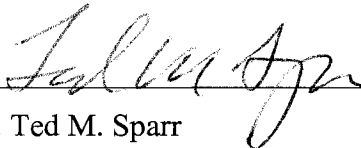
Dr. Marc R. Lessard

Research Associate Professor of Physics



Dr. R. Daniel Bergeron, Thesis Director

Professor of Computer Science



Dr. Ted M. Sparr

Professor of Computer Science

Aug. 15. 2008

Date

ACKNOWLEDGEMENTS

I would like to thank

My research advisor, Professor Marc R. Lessard, for his patience in guiding my academic progress. He introduced me to a variety of experiences in my research field such as space physics and space instrumentation background. My view of space physics has been deepened by his encouragement.

My academic advisor, Professor R. Daniel Bergeron for being my thesis committee member as the thesis director, for discussions on my thesis and scientific visualization, and for guidance on my academic work. He also helped me a lot to find many research-related reference materials and work.

Professor Ted M. Sparr for being one of my thesis committee members. His profound knowledge on scientific database has inspired me to keep my thesis topic on the right track.

Sarah Jones, Paul Riley, Brent Sadler, and all people in the Magnetosphere-Ionosphere Research Laboratory for their help and encouragement.

Especially, my brother, Hyomin Kim, for his patience in guiding my academic and research work, my parents for their love and guidance, and my parents in law for their love and support.

Finally, my wife, Heesung, for her inestimable love and support in many ways, without which my study as well as the completion of my thesis would not be possible.

TABLE OF CONTENTS

ACKNOWLEDGEMENTS	iii
LIST OF TABLES	vi
LIST OF FIGURES	vii
ABSTRACT.....	xi

CHAPTER	PAGE
1 INTRODUCTION	1
1.1 Background and research goal	1
1.2 Satellite observation of auroral emission	2
1.3 Satellite measurement specification.....	4
2 TOMOGRAPHY OVERVIEW	7
2.1 Basic tomography using parallel projection	7
2.2 Algebraic Reconstruction Methods.....	10
2.3 Overall reconstruction process.....	14
3 IMPLEMENTATION OF IMAGE RECONSTRUCTION	17
3.1 Overview.....	17
3.2 Beam-pixel clipping for weighting factor.....	17
3.3 Algorithm description	21
3.4 Results.....	23

4	SATELLITE-BASED 3D VOLUME RECONSTRUCTION.....	27
4.1	Constraints	27
4.2	Coordinate transformations between optical instrument and volume.....	30
4.3	Beam tracing weighting factor approximations.....	32
4.4	Optimizing approximations	35
4.5	Algorithm description	35
4.6	Results.....	39
4.7	Conclusion	46
5	ADAPTIVE TIME-VARYING VOLUME RECONSTRUCTION.....	49
5.1	Motivation.....	49
5.2	Auroral measurement.....	50
5.3	Method.....	51
5.4	Results.....	55
5.5	Conclusion and future work.....	60
	LIST OF REFERENCES.....	63

LIST OF TABLES

Table 1: FAI two imagers of e-POP satellite [27]	5
Table 2: Solving a set of unknown pixels using ART	13
Table 3: Several weighting factor results between two methods.....	34
Table 4: Similarity and similarity ² of the original volume and the reconstructed volume using different approximations	44
Table 5: Similarity between the original and reconstructed volumes above	56
Table 6: Similarity changes between time-varying original and reconstructed volumes using ART.....	58
Table 7: Similarity changes between time-varying original and reconstructed volumes using ART.....	59

LIST OF FIGURES

Figure 1: Auroral emission (mostly 557.7 nm), photo by Hyojin Kim, at the Poker Flat Research Range in Fairbanks, Alaska, US.....	3
Figure 2: FAI target acquisition mode (fixed focal point) for auroral volume reconstruction.....	6
Figure 3: 2D to 1D parallel projection representation and algebraic approaches.....	9
Figure 4: Solving a linear system on a hyperplane (a) Solving a solution of two linear equations using an iterative method of projections (b) Solving an approximate solution of three linear equations.....	12
Figure 5: An example of a unknown source image with four observed ray-sums by two projections.....	13
Figure 6: Weighting factors as coefficients	15
Figure 7: Different weighting factor approximations (a) Binary sampling approximations using ray-cell intersection (top) and using ray-cell distance (bottom) (b) Our beam-pixel clipping	20
Figure 8: Image (volume slice) reconstruction results with parallel projection (a) original images (b) reconstructed images using binary sampling approximation (ray-cell intersection) (c) reconstructed images using binary sampling approximation (ray-cell distance) (d) reconstructed images using beam-pixel clipping.....	24
Figure 9: Image reconstruction results using ART and MART method with different projections.....	26

Figure 10: Unnecessary pixels during image measurement of auroral zone	29
Figure 11: Coordinate transformation for satellite-based auroral volume reconstruction	31
Figure 12: Main process of the coordinate transformations in auroral volume reconstruction.....	31
Figure 13: Beam tracing approximations in perspective projection	32
Figure 14: Two beam tracing approximations (a) Beam-voxel clipping (b) Beam-voxel sampling.....	33
Figure 15: Verification of our algorithm using volume rendering and volume reconstruction.....	37
Figure 16: Our volume rendering and volume reconstruction application.....	39
Figure 17: Different weighting factor approximation results of 32^3 volume (a) Beam-voxel sampling (binary) (b) Beam-voxel sampling (2^3) (c) Beam-voxel sampling (4^3) (d) Beam-voxel clipping	41
Figure 18: Representative volume slices ($z=16$) and pixel distributions ($y=10, 11, 12$) of Figure 17 (1) (a) Original volume (b) Beam-voxel sampling (binary) (c) Beam-voxel sampling (2^3) (d) Beam-voxel sampling (4^3) (e) Beam-voxel clipping	42
Figure 19: Different weighting factor approximation results and representative slices of 64^3 volume (a) Original volume (b) Beam-voxel sampling (binary) (c) Beam-voxel sampling (2^3) (d) Beam-voxel sampling (4^3) (e) Beam-voxel clipping.....	42
Figure 20: Different weighting factor approximation results and representative slices of gradient 32^3 and 64^3 volumes (a) Original volume (b) Beam-voxel sampling (binary) (c) Beam-voxel sampling (2^3) (d) Beam-voxel sampling (4^3) (e) Beam-voxel clipping.....	43

Figure 21: Reconstructed volumes and the similarity results using different focal points	
(a) Original volume	
(b) Reconstructed volumes with a focal point outer of the volume (-0.5)	
(c) Reconstructed volumes with a focal point near bottom (0.0)	
(d) Reconstructed volumes with a focal point in the volume center (0.5).....	45
Figure 22: Time-varying auroral motion and satellite measurement.....	51
Figure 23: Minimum projection (measurement) angle	52
Figure 24: Time-varying multi-volume reconstruction in a single orbital path.....	53
Figure 25: The voxels of the previous reconstructed volume as initial guesses for the next reconstruction.....	54
Figure 26: Preprocess of time-varying auroral volume reconstruction	55
Figure 27: Original and reconstructed 64^3 volumes using ART with different projection angles (a) 60° (b) 80° (c) 100° (d) 120° (e) 140° (f) 160°	55
Figure 28: Time-varying volume reconstruction test.....	57
Figure 29: Time-varying reconstructed volumes using ART (a) 00:05:00 (300 sec) (b) 00:05:50 (350 sec) (c) 00:06:40 (400 sec) (d) 00:07:30 (450 sec) (e) 00:08:20 (500 sec) (f) 00:09:10 (550 sec) (1) Original volumes (2) A reconstructed volume with 180° projection angle (3) Reconstructed volumes with 120° projection angle (4) Reconstructed volumes with 100° projection angle (5) Reconstructed volumes with 80° projection angle (6) Reconstructed volumes with 60° projection angle	57
Figure 30: Original and reconstructed volumes with a representative volume slice ($z=2$)	
(a) Volumes at 50 sec	
(b) Volumes at 90 sec	
(c) Volumes at 130 sec (1) Original volumes (2) A reconstructed volume with 180° projection angle (3) Reconstructed	

volumes with 100° projection angle	(4) Reconstructed volumes with 80° projection angle	
angle	(5) Reconstructed volumes with 60° projection angle	59
Figure 31: Time-varying adaptive volume positioning		61
Figure 32: Parallel time-varying volume reconstruction		62

ABSTRACT

SATELLITE-BASED AURORAL TOMOGRAPHY AND TIME-VARYING VOLUME RECONSTRUCTION

by

Hyojin Kim

University of New Hampshire, September, 2008

Tomography, originally developed to observe the internal structure of a human body in medical applications, can also be applied to research in Space Science applications. An upcoming satellite mission incorporates two imagers for auroral observation in the upper atmosphere. For this mission, development of auroral volume reconstruction using tomographic imaging is useful for understanding the internal structure of auroras. We have shown that beam-pixel clipping in image reconstruction improves the quality of reconstructed images, compared to previous techniques. The goal is to develop a suitable algorithm for auroral volume reconstruction using auroral images measured from satellite-borne optical instruments. We have demonstrated that weighting factor approximation in algebraic methods plays a crucial role in the quality of volume reconstruction. We also have evaluated the effectiveness of this algorithm with measured images of known volumes using perspective projections. In addition, a time-varying volume reconstruction scheme is discussed where auroras move over time.

CHAPTER 1

INTRODUCTION

1.1 Background and research goal

Tomography (i.e., Computerized Tomography; CT) or cross-sectional imaging is a useful technique for observing the internal structure of a source of unknown composition. Tomographic imaging techniques which were originally developed for medical applications can also be applied to research on the upper atmosphere of the earth using ground-based observatories and satellite instruments. The upcoming Canadian Enhanced Polar Outflow Probe (e-POP), a scientific multi-purpose satellite mission, incorporates two auroral imagers for the observation of auroral arc emission in the ionosphere. For this particular mission, development of an auroral volume reconstruction based on tomographic imaging methods is useful for understanding the internal structure of the auroral arc which is not yet clearly known.

The main goal of this research is to develop a suitable algorithm to reconstruct 3D auroral volumes using sequences of auroral images from the e-POP imagers. Volume reconstruction using optical imaging instruments provides some challenges and opportunities that differ from those of traditional medical applications based on X-ray parallel projection. We discuss geometric calculations of parameters for algebraic reconstruction methods such as perspective projection (fan beam geometry), field of view

(FOV), and image resolution; our algorithm utilizes these optical characteristics to improve the reconstruction process. Our scheme can also be applied to various volume reconstruction application using images measured from ground-based observatories or other optical measurements. In addition, where there is a case that aurora arcs are drifting during the image acquisition, a time-varying volume reconstruction scheme can also be used.

1.2 Satellite observation of auroral emission

Auroral emission results from the excitation and ionization of atmospheric constituents with precipitating energetic particles. Atoms and molecules in the upper atmosphere of the earth collide with the incoming auroral particles from outer space (i.e., solar wind). The kinetic energy of the collision gives rise to the change of the chemical state of those atoms and molecules from the original state into an excited state. When they are transited into the original state (ground state), the energy releases photons of particular wavelengths and it causes the auroral emission [19].

Generally an aurora contains a number of spectral lines and bands in the optical spectrum. It varies from ultraviolet to infrared wavelengths [19]. The spectrum depends on the type of the primary constituents in the upper atmosphere and the energy level of precipitating particles. For example, green emissions at 557.7 nm wavelength and red emissions at 630.0 nm are related to oxygen atoms and their excited state [7]. The green oxygen line is a dominant wavelength in the region, which is the most sensitive to the human eye [19]. The following Figure 1 is an example of auroral emission mostly with green colors.

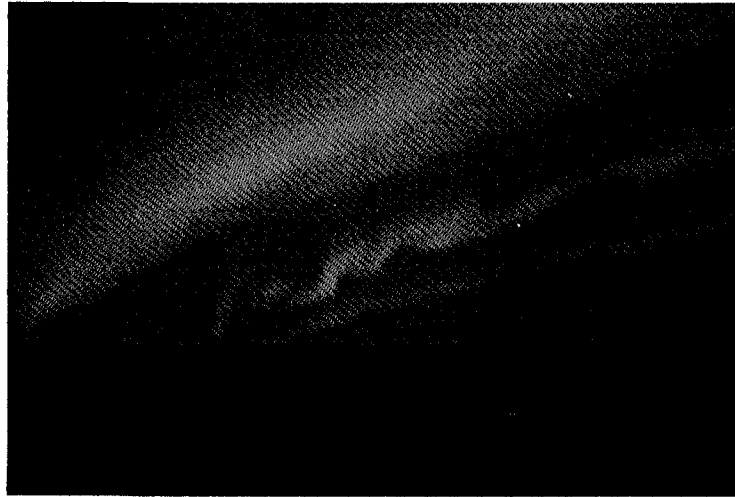


Figure 1: Auroral emission (mostly 557.7 nm), photo by Hyojin Kim, at the Poker Flat Research Range in Fairbanks, Alaska, US

The importance of auroral emission observation is that it is closely related to solar activity. During periods known as magnetic storms, a large number of electrically charged particles from the sun (i.e., solar wind) enter the upper atmosphere of the earth (e.g., ionosphere, magnetosphere), which makes auroras widespread [7]. In addition, these solar activities cause a lot of other events that occur in the upper atmosphere around the earth such as substorms and MHD waves. In general, we study aurora because it is one way of understanding low energy in the solar wind transferred to our upper atmosphere.

One of characteristics of aurora is that it moves and changes form at various speeds and rates. Mostly, warping of the precipitating energetic particle streams by the magnetic and electric fields causes the auroral motions and changes [7]. According to the scale of the motion, it can be classified as global-scale motions, large-scale motions and small-scale motions. The speed of the global-scale auroral motions is somewhat less than a kilometer per second, but most actual motions are much faster. In small-scale auroral motions such as the motion of rays along auroral forms, the speed is generally faster

(approximately tens of kilometers per second) than those of global-scale and large-scale motions [7]. If auroral arcs drift and change fast, a set of auroral images taken from a remote measurement (such as e-POP image output) cannot be used for an accurate auroral volume reconstruction. In order to perform a reconstruction, auroral arcs should be stationary or move very slowly. Otherwise, a time-varying reconstruction algorithm can be considered.

1.3 Satellite measurement specification

The e-POP payload has eight scientific instruments including an imaging ion mass spectrometer, a suprathermal electron imager, a GPS attitude & profiling experiment and a fast auroral imager. These instruments will collect various data on space storms and associated plasma outflows in the upper atmosphere. Among these instruments, the Fast Auroral Imager (FAI) will be used to acquire images of auroral arc emission [27].

FAI is a dual CCD/single controller camera that will image the topside aurora in the region of the spacecraft's magnetic footprint. The two optical imaging channels provide a narrowband image (630.0 nm) with 128×128 pixels (FAI-SV), and a broadband image from 650-1100 nm (infrared) with 256×256 pixels (FAI-SI). The image rate is 10 images per second in the NIR band and 1 image per minute at 630 nm. The two imager channels have identical optics, with FOV of 20°×27°, but use different filters. Since the orbit of e-POP will have a nominal perigee of 315 km and an apogee of 1500 km, the imager will have an effective spatial resolution of 2.6 km at apogee. The FAI-SV will provide coverage of 380×380 km at 1000 km altitude, while the FAI-SI will provide

coverage of 430×430 km [27]. The following Table 1 summarizes the specification of the two imagers.

	FAI-SV	FAI-SI
Bandwidth	630.0 nm	650 - 1100 nm
FOV	27°	27°
Coverage (at 1000km)	380 × 380 km	430 × 430 km
Resolution	128 × 128	256 × 256
Framerate	2 frames/min	1 frame/sec
1-path frame rate	4 - 30 frames	120 - 900 frames

Table 1: FAI two imagers of e-POP satellite [27]

As mentioned previously, even “stationary” auroral arcs can change at a speed of a few kilometers per second. But in some cases, changes and fluctuations at a rate may also take place very rapidly. Therefore in order to reconstruct an auroral volume (or a set of volumes) in a certain time period, images only in a single orbital path will be available. It will take approximately from 2 to 15 minutes to take a set of images in one path in the orbit of the e-POP satellite, depending on the precise altitude of the satellite. Table 1 also shows the 1-path frame rate for both imagers. Because the two imagers in FAI have a different resolution and frame rate, the resolutions of possible reconstructed volumes vary. This is discussed on the chapter on “Time-varying volume reconstruction.”

To reconstruct the volume of auroral arcs, a set of images, all of which point to a fixed or limited focal target of an auroral zone, is needed. FAI imagers will be set to a target acquisition mode as shown in Figure 2. In the target acquisition mode in each orbital path, the imagers will point to a limited auroral zone to take a set of auroral images. Since the focal point of the imagers can vary within the auroral zone, each acquired image will include its target position, instrument position, and instrument roll information usually determined by the attitude control system or star-sensor of the satellite.

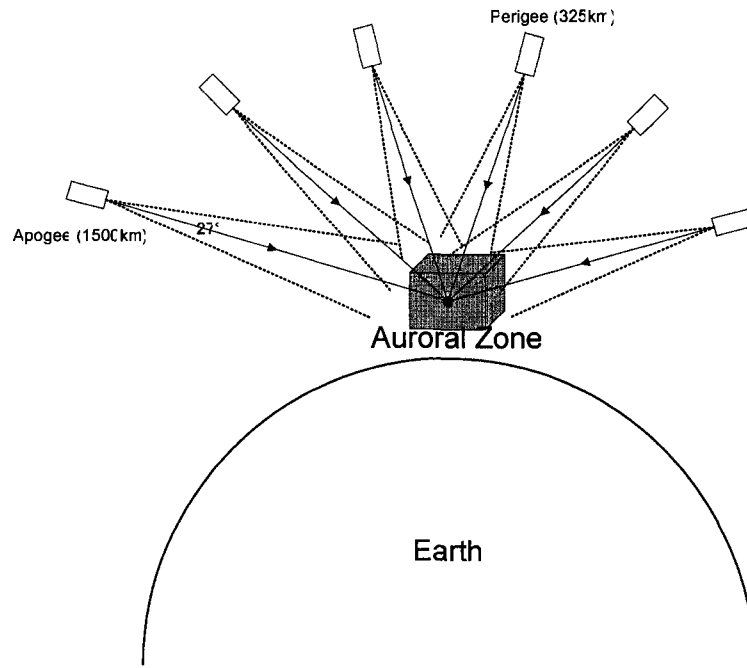


Figure 2: FAI target acquisition mode (fixed focal point) for auroral volume reconstruction

CHAPTER 2

TOMOGRAPHY OVERVIEW

2.1 Basic tomography using parallel projection

Tomography (i.e., Computerized Tomography) was originally developed for medical applications to obtain a set of images of internal structures of a human body. Because the reconstructed images show unknown internal structures of a body or organs in a particular plane, this technique is referred to as cross-sectional imaging. In medical applications, those cross-sectional images are generated from a set of X-ray images in a wide angle of projections [18].

The source distributions are generally represented as 2D images or 3D volumes, depending on the number of dimensions of the observed data. In principle, a set of $(n-1)$ -dimensional remote measurements is needed in order to reconstruct an unknown n -dimensional source [12].

We present a simple case of an image reconstruction (2D) of an unknown source using a set of projections (1D) as shown in Figure 3. This is a simplification (one volume slice reconstruction) of medical CT scanning using X-ray projections. In each projection, a number of rays are sent from a transmitter on a side and are detected by a receiver on the other side. There is an assumption that each ray path is parallel, just as X-ray projection, and there is no refraction and diffraction effect [18]. Once a projection is

completed, which consists of a number of ray-sums (i.e., ray-intensity along a path), another projection with a different angle is performed.

The unknown source area is uniformly divided into small cells in a 2D image plane. Each cell value (X_i) represents the ray intensity of the cell. In this example, the unknown image has 5×5 pixels and there are 4 rays in a projection. The goal of tomography is to solve for the unknown values of the 5×5 cells using mathematical methods. Various tomographic techniques have been proposed and developed. These can be classified into 5 groups [12, 18, 25]:

- *image-Fourier space methods (Fourier transform methods)*
- *image-projection space methods (algebraic methods)*
- *deconvolution-restoration approaches*
- *reflection tomography*
- *statistical methods*

Among these methods, image-projection space methods (i.e., algebraic methods) are the most appropriate where: 1) it is difficult to measure a large number of projections, 2) the projections are not uniformly distributed, 3) or the angle of the projections is narrow (limited-view) [18]. For example, in medical diagnostics, some patients cannot be exposed to the amount of radiation normally used for a complete scan; these techniques are applicable where it is necessary to limit the radiation dosage [26]. In our case, also, the projection angle is much less than 180° . Even if the projection angle can be around 180° , some images taken near or on the horizon will probably not be good quality auroral pictures and may contain other external noise.

For such cases, many studies have shown that several algebraic methods produce better results than other techniques including Fourier transform methods [15, 18]. We now present a brief overview of algebraic methods for reconstructing 2D images using 1D parallel projections. This is a simplified version (i.e., one image-slice reconstruction) of a real 3D volume reconstruction using 2D images generated by parallel projections.

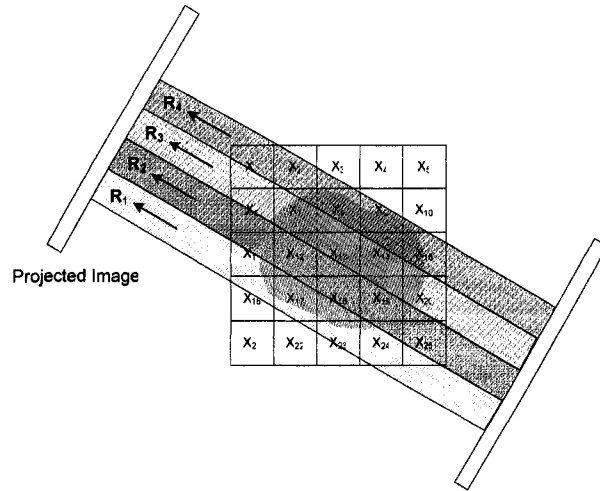


Figure 3: 2D to 1D parallel projection representation and algebraic approaches

In Figure 3, the source area is divided into N cells where each cell has the same size; X_i represents an unknown variable to be calculated as mentioned above. Each ray-sum (R_1 to R_4) is projected onto a pixel on the projected image. In algebraic methods, each projected ray can be represented as the sum of some cells as a linear equation where the weighting factor, W_i , indicates the contribution ratio of the cell to the ray ($0 - 1$). This is represented as a set of linear equations:

$$\begin{aligned}
 W_{1(R1)}X_1 + W_{2(R1)}X_2 + \dots + W_{25(R1)}X_{25} &= R_1 \\
 W_{1(R2)}X_1 + W_{2(R2)}X_2 + \dots + W_{25(R2)}X_{25} &= R_2 \\
 W_{1(R3)}X_1 + W_{2(R3)}X_2 + \dots + W_{25(R3)}X_{25} &= R_3 \quad (1) \\
 \dots &
 \end{aligned}$$

Since the number of cells is 25 in this example, at least 25 different linear equations are needed. In its matrix form, direct matrix inversions such as Gauss-Jordan elimination and LU decomposition can be employed to solve the unknown cell values [24]. However, it is computationally expensive because the number of cells is generally large. In practice, it is at least 4,096 (64×64), 16,384 (128×128), or 65,500 (256×256) [18]. In 3D volume reconstruction, the complexity of matrix inversion exponentially increases. There are more reasons why direct matrix inversions are not appropriate; it is also possible that 1) the set of the linear equations is sparse (too many 0's in the weighting factors), 2) the matrix is singular, or 3) the matrix is not square. Especially, there are many situations in which the number of ray-sums is not the same as the number of cell values (X 's). In these cases, direct matrix inversion is impossible. If the number of ray-sums is exactly the same as the number of unknown cells, there is a possibility of direct matrix inversion. But the issue regarding computational complexity still remains. Other problems occur because a set of ray-sums contain some noise and typical weighting factors are not very accurate; we discuss these issues in more detail below. There are iterative approximation methods that offer an approximate solution as the iterative procedure continues. Since these methods solve all possible cases mentioned above, they are much more appropriate than direct matrix inversion methods.

2.2 Algebraic Reconstruction Methods

“Algebraic Reconstruction Techniques” (ART) are based on “Method of Projections” by Kaczmarz and Tanabe [18] and “Back-Projection” by Budinger and Gullberg [12]. In these methods, the iteration is started with a set of initial cell values [18]. As the iteration continues, the cells are updated and converge to an approximate

solution for the cell values. According to [15], there are several advantages of this approach over the Fourier transform methods:

- algebraic methods work properly for totally asymmetric objects;
- they produce detailed and better results with only 5 – 10 views;
- tilting techniques may be used since the views may be taken over a small range of angles ($\pm 30^\circ$);

- small computers with a small amount of storage and resources can be used.

In this sense, the algebraic approach is the most appropriate solution for the auroral tomography and volume reconstruction.

The basic idea of ART is to use convergence by projections where the linear system is represented as a hyperplane (i.e., $n - 1$ dimensional subspace in an n -dimensional vector space) [18]. Solving a unique solution of two linear equations is a simple example as shown in Figure 4 (a). The two linear equations are:

$$W_{1(R1)} X_1 + W_{2(R1)} X_2 = R_1$$

$$W_{1(R2)} X_1 + W_{2(R2)} X_2 = R_2 \quad (2)$$

And those equations can also be represented as the following vectors:

$$W_{(R1)} \cdot X = R_1 \quad (3)$$

$$W_{(R2)} \cdot X = R_2 \quad (4)$$

The method is started with an initial guess of X , denoted by $X^{(0)}$. In this case, a set of initial values for $X^{(0)}$ is $(0, 0)$. On the first iteration, the initial vector $X^{(0)}$ is projected onto the line of the first equation (3). The projected vector, denoted by $X^{(1)}$, should be perpendicular to the equation. $X^{(1)}$ becomes a new vector of X updated by the first iteration. On the next iteration, the new vector $X^{(1)}$ is projected onto the second equation

(4). The vector is then updated to a new vector $\mathbf{X}^{(2)}$ on the second line. These iterations are repeated until the set of values (vector \mathbf{X}) converges to a unique solution as shown in the figure.

Figure 4 (b) illustrates solving an approximate solution of three linear equations. In this case, since there is not a unique solution, we need to settle for an approximate solution. Similar to Figure 4 (a), the method makes the set of values oscillate in the neighborhood of an approximate solution [18]. It is useful where the number of equations is greater than the number of cell values.

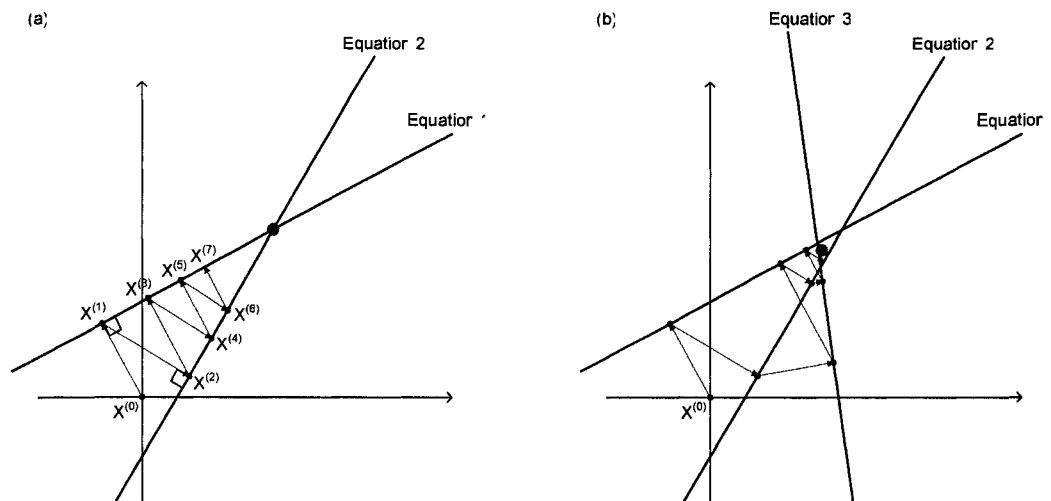


Figure 4: Solving a linear system on a hyperplane (a) Solving a solution of two linear equations using an iterative method of projections (b) Solving an approximate solution of three linear equations

The basic ART can be mathematically written as follows [18]:

$$\mathbf{X}^{(i)} = \mathbf{X}^{(i-1)} + \frac{\mathbf{R}^{(i)} - \mathbf{X}^{(i-1)} \cdot \mathbf{W}^{(i)}}{\sum \mathbf{W}^{(i)2}} \mathbf{W}^{(i)} \quad (5)$$

where \mathbf{X} is a vector of unknown cell values, \mathbf{W} is a vector of weighting factors, \mathbf{R} is a measured ray-sum, and i is an iteration number from 1. $\mathbf{X}^{(0)}$ is a vector of initial values, $(0, 0, \dots, 0)$ in most cases. The initial values are updated by adding the next

perpendicular vector to the current values and the values are updated in the following iterations. It is an additive method, and therefore it is also called Additive ART.

Figure 5 shows a 2x2 unknown source where the values are represented as the vector (1, 2, 3, 4). There are also four observed ray-sums ($R^{(1)}$, $R^{(2)}$, $R^{(3)}$ and $R^{(4)}$) by two projections. Since all rays are horizontal or vertical, weighting factors are exactly equal to 0 or 1. For example, in $R^{(1)}$, the weighting factor of X_1 and X_2 are 1 while the weighting factor of X_3 and X_4 are 0. Table 2 shows that the ART method updates a set of values and these values converge to a solution which is the same as the original source.

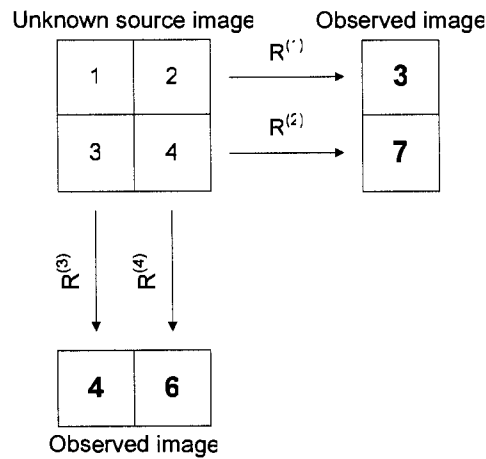


Figure 5: An example of a unknown source image with four observed ray-sums by two projections

Iteration Number	R	W	X
0			(0.0, 0.0, 0.0, 0.0): Initial Values
1	3	(1, 1, 0, 0)	(1.5, 1.5, 0.0, 0.0)
2	7	(0, 0, 1, 1)	(1.5, 1.5, 3.5, 3.5)
3	4	(1, 0, 1, 0)	(1.0, 1.5, 3.0, 3.5)
4	6	(0, 1, 0, 1)	(1.0, 2.0, 3.0, 4.0)

Table 2: Solving a set of unknown pixels using ART

The above example is a simple case to solve a solution using ART. But if the weighting factors, W , are poorly calculated, ART reconstructions cause “salt and pepper noise” [18]. In most cases, the weighting factors are usually inaccurate approximations

and the ray-sums may also be poorly measured. These problems lead to various modifications such as the Multiplicative ART (MART), the Simultaneous Iterative Reconstructive Technique (SIRT), and the Simultaneous Algebraic Reconstruction Technique (SART). The basic MART is described as [21]:

$$\mathbf{X}^{(i)} = \mathbf{X}^{(i-1)} \cdot \left(\frac{\mathbf{R}^{(i)}}{\mathbf{X}^{(i-1)} \cdot \mathbf{W}^{(i)}} \right)^{\mathbf{w}^{(i)}} \quad (6)$$

Usually, $(e^{-1}, e^{-1}, \dots, e^{-1})$ is chosen for the initial vector $\mathbf{X}^{(0)}$. MART is likely to produce less noise than ART since once a cell value is set to 0, it cannot be updated. While both ART and MART update the cell values iteratively on a ray-by-ray basis, SART updates the cell values after a whole image projection is completed. For more details about the characteristics of these methods, see [6].

2.3 Overall reconstruction process

As mentioned before, a set of observed 1D images is needed to reconstruct an unknown 2D image in this example. Solving for the unknown pixels of the 2D image using linear equations from the 1D images in iterative algebraic methods is the main goal of this tomography. The size of the reconstructed image depends on the number of linear equations provided. Thus, the number of equations should be at least the number of pixels of the reconstructed image. The number of equations depends on the number of projections and the size of each 1D image. In short, once the size and the number of the 1D projected images are determined, the number of pixels (the size of the reconstructed image) is determined.

Each linear equation needs a set of weighting factors, coefficients of the equation, determined by one of rays of the 1D projected images. Each cell's weighting factor is the ratio of the ray's contribution to the cell. Conceptually, in a geometric sense, the

weighting factor is the ray-intersected area divided by the entire area of each cell as shown in Figure 6. In this example, X_2 's weighting factor is 0 because the ray doesn't contribute to the cell. The weighting factor varies between 0 and 1, but most factors are 0 and the linear equations are sparse.

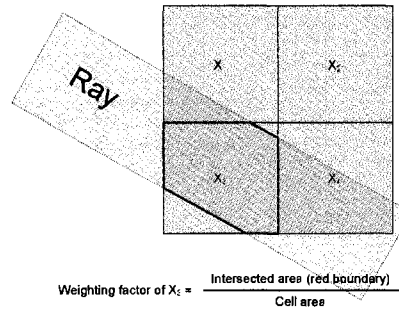


Figure 6: Weighting factors as coefficients

In real applications, where the reconstructed 2D image is 64×64 and it is assumed that there are enough linear equations for the reconstruction, the number of weighting factors for each equation becomes 64×64 . If the number of equations is 100, the total number of weighting factors to be calculated becomes $64 \times 64 \times 100$, which needs a huge computation time and resources (memory or storage). For this reason, some approximations to calculate the weighting factors are recommended. Many applications use binary approximation, in which the factors are simply replaced by 1's and 0's, which makes the implementation easier and reduce computation time and resources [18].

Here is an overall description for the simple reconstruction application above. First, a set of 1D images are acquired. Depending on the number of the images and each image's size (i.e., the number of rays), the size of a 2D image to be reconstructed is determined. Then the initial values are assigned to all cells. If the basic additive ART is being used, the initial cell values are 0 and the iterations are started with the values. Next, the first 1D image is chosen and the first pixel of the image is used for the first ray. Using

the current projection information (e.g., angle, position) and the ray, a set of weighting factors is calculated. Once a set of factors is determined, a linear equation is prepared and it is applied to the iterations. Then the next pixel of the image is used for the second ray and a set of weighting factors for the ray is calculated. This same process is repeated until all observed 1D images are used. As the iteration goes on, the cell values converge to an approximate solution and a reconstructed 2D image is completed.

CHAPTER 3

IMPLEMENTATION OF IMAGE RECONSTRUCTION

3.1 Overview

In this chapter, we describe an implementation of image reconstruction that motivates and helps describe our volume reconstruction described in the next section. The implementation is based on tomographic imaging methods using several Algebraic Reconstruction Techniques. For 2D image reconstruction, 1D measured images with multiple projections are used. This implementation includes 1D observed image generation by an arbitrary projection, several approximations of weighting factors including a clipping algorithm, two different ART methods (Additive ART and Multiplicative ART), and an interactive environment so that users can perform various projections and reconstructions with different options.

3.2 Beam-pixel clipping for weighting factor

As mentioned before, in most cases, fast but poor approximations of weighting factors are used to reduce computational time and resources. In some applications, each weighting factor is approximated by a function of the perpendicular distance between the center of each ray and the center of each cell and these factors are replaced with 0's and 1's [18]. For instance, if the distance is smaller than the half size of the cell, the weighting factor becomes 1. Another approximation, suggested by [26], uses the length

of the intercept of the center of each ray with each cell. If there is an intersection, the weighting factor of the cell is 1, otherwise it is 0. This approximation is slightly different from the approach taken by [18] where the ray is tilted and it intersects slightly the outline of a cell, and the weighting factor of the cell becomes 1. Such fast but poor binary sampling approximations are easy to implement, but may result in low quality reconstructed images with significant noise called “salt and pepper noise”. There have been various mathematical attempts using modified ARTs to suppress such noise and to improve the quality of reconstructed results with smoothness. Some cases use a relaxation parameter to prevent faster convergence in ART reconstructions. Although this approach offers noise reduction, it increases the number of iterations. Other approaches put more emphasis on mathematical methods to modify ART, such as MART and SART [18].

Instead of such mathematical approaches, in this paper we focus on the geometric nature of ray projections to more accurately compute weighting factors. We propose a better approximation, called beam-pixel clipping that produces higher quality reconstructed images and volumes. Conceptually, if the ray in 2-D is modeled as an area (instead of a line), the weighting factor can be represented as the ray-intersected area divided by the entire area of the cell. In image reconstruction, our approach uses a classic polygon clipping algorithm, Sutherland-Hodgman clipping, in order to calculate the clipped ray-polygon area accurately. Thus this approximation is the same as the conceptual weighting factor calculation. Since this clipping algorithm is fast and efficient in 2D graphics [3], it is not computationally expensive. In each ray projection, the ray is represented as a long rectangular area, “beam”, which is clipped against each rectangular

cell. In volume reconstruction described in Section 4, each ray is represented as a long pyramidal beam, which is clipped against each voxel.

Figure 7 shows several different approximations. Figure 7 (a) are the two binary approximations mentioned above. The left-top of Figure 7 (a) shows the approach taken by [26] and the left-bottom of Figure 7 (a) shows that of [18]. In the left-top figure, since the center line of the ray intersects X_3 and X_4 , the weighting factors of X_3 and X_4 are 1 even though both of them are not truly 1. On the other hand, since the center line of the ray doesn't intersect either X_1 or X_2 , both factors are 0 even though the factor of X_1 is not truly 0 as shown in the figure. Such approximations are computationally cheap and fast, but they may cause poor results with some error and noise.

Figure 7 (b) describes our beam-pixel clipping method. The actual beam polygon of the ray is used for clipping with each rectangular cell. In each cell, the clipping with the beam is processed and a clipped beam polygon of the ray is generated. The weighting factor of each cell is the ratio of the beam's clipped area to the cell's area. We demonstrate that this approach provides more accurate weighting factors and better reconstructed images than the binary approximations.

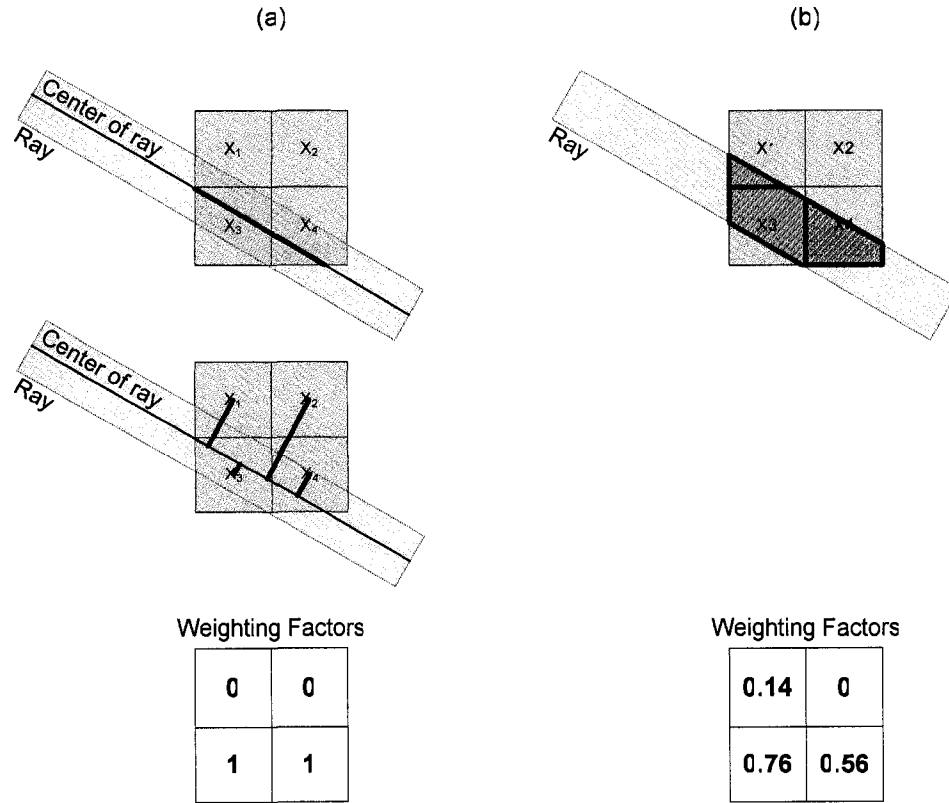


Figure 7: Different weighting factor approximations (a) Binary sampling approximations using ray-cell intersection (top) and using ray-cell distance (bottom) (b) Our beam-pixel clipping

As mentioned before, Sutherland-Hodgman Polygon Clipping is used for computing more accurate weighting factors. See [3] for detailed discussion of this clipping algorithm. Once a clipped polygon of the ray is generated, the area of the polygon is calculated using the following equation:

$$Area = \sum_{i=0}^{n-1} (X_i Y_{i+1} - Y_i X_{i+1}) \quad (7)$$

Where the clipped polygon has points $(X_0, Y_0) \dots (X_n, Y_n)$ [2].

3.3 Algorithm description

The implementation of 2D image reconstruction basically consists of two steps:

- The program reads an original 2D image. Using the image, a projected 1D image with an arbitrary angle is generated.

- The program prepares an empty 2D image for the reconstruction with initial pixel values. Using the projected 1D image, the program starts iteration of ART and the initial 2D image is updated.

Once the two steps are completed, the next 1D image projection and its iteration are repeated until the program processes enough projections and iterations. In real applications, the first step is not necessary since a set of projected 1D images should already be prepared. In this case, the 1D images should have some associated metadata information, including the angle of the projection and the number of pixels (rays). Once an image reconstruction is completed, the reconstructed image can be compared with the original image in order to verify our reconstruction algorithm.

The following is the pseudo code of the main reconstruction process:

Create an empty 2D image

Initialize the image with initial pixel values

FOR *each 1D image projection*

Load camera information of this projection (angle, position, etc)

Get the number of rays for this projection

FOR *each ray of this projection*

Get the ray-sum

Create a ray polygon

FOR *each pixel (x, y) of the 2D image*

(the number of 2D image pixels)

Compute the weighting factor

(using beam-pixel clipping, binary sampling, etc)

ENDFOR *of each pixel*

Set a linear equation

Update the pixel values of the 2D image using ART, MART, etc

ENDFOR *of each ray*

ENDFOR *of each 1D image projection*

3.4 Results

Figure 8 shows several reconstructed results according to different approximations. The original and reconstructed images are 128×128 8-bit grayscale bitmaps. All these image reconstructions were processed using the basic additive ART method. All reconstruction tests used 140 ray projections, each with 160 rays. The angular range of the projections is 140° (0° to 140°). We created several artificial images with easily identifiable characteristics; the original images are shown in column (a) of Figure 8. Row (1) is intended to represent simplified auroral arcs; row (2) adds some Gaussian blurring; row (3) and (4) are intended to represent more complex visual phenomenon. The images in column (b) were reconstructed using binary sampling approximation with a line intercept method while the images in column (c) were generated using binary sampling approximation with a line-cell distance method. Column (d) shows our beam-pixel clipping.

A quantitative method to compare the original image with the reconstructed image is useful to evaluate the performance of these approximations. We used a similarity function, taken by [10], to measure the differences (error) between each original value and its corresponding reconstructed value. The function can mathematically be written as:

$$Similarity = 1 - \sqrt{\frac{\sum (V_R - V_O)^2}{\sum V_O^2}} \quad (8)$$

where V_R and V_O are pixel values of the original and the reconstructed image. If the similarity is equal to 1, two images are identical. Otherwise, the similarity is always less than 1. Images in column (d) are smooth and look somewhat more like the original

images while the other reconstructed images seem to contain more noise. The results show that our beam-voxel clipping improves the quality of reconstruction and reduces noise. In this result, All reconstructed images somewhat slant to the left. It seems related to the direction of the projection. The shape of reconstructed images can vary depending on which direction the projection rotates and when the images are mainly converged.

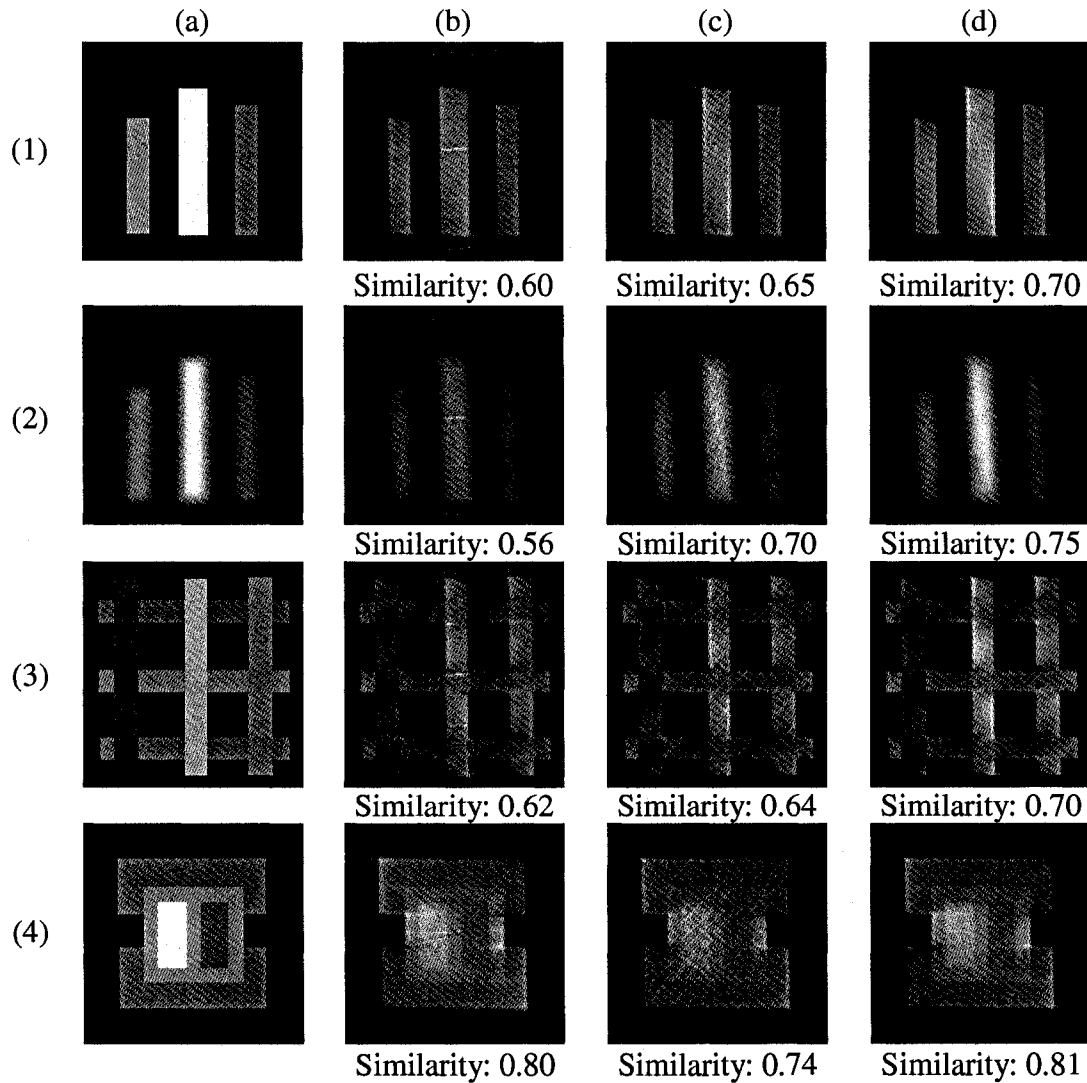
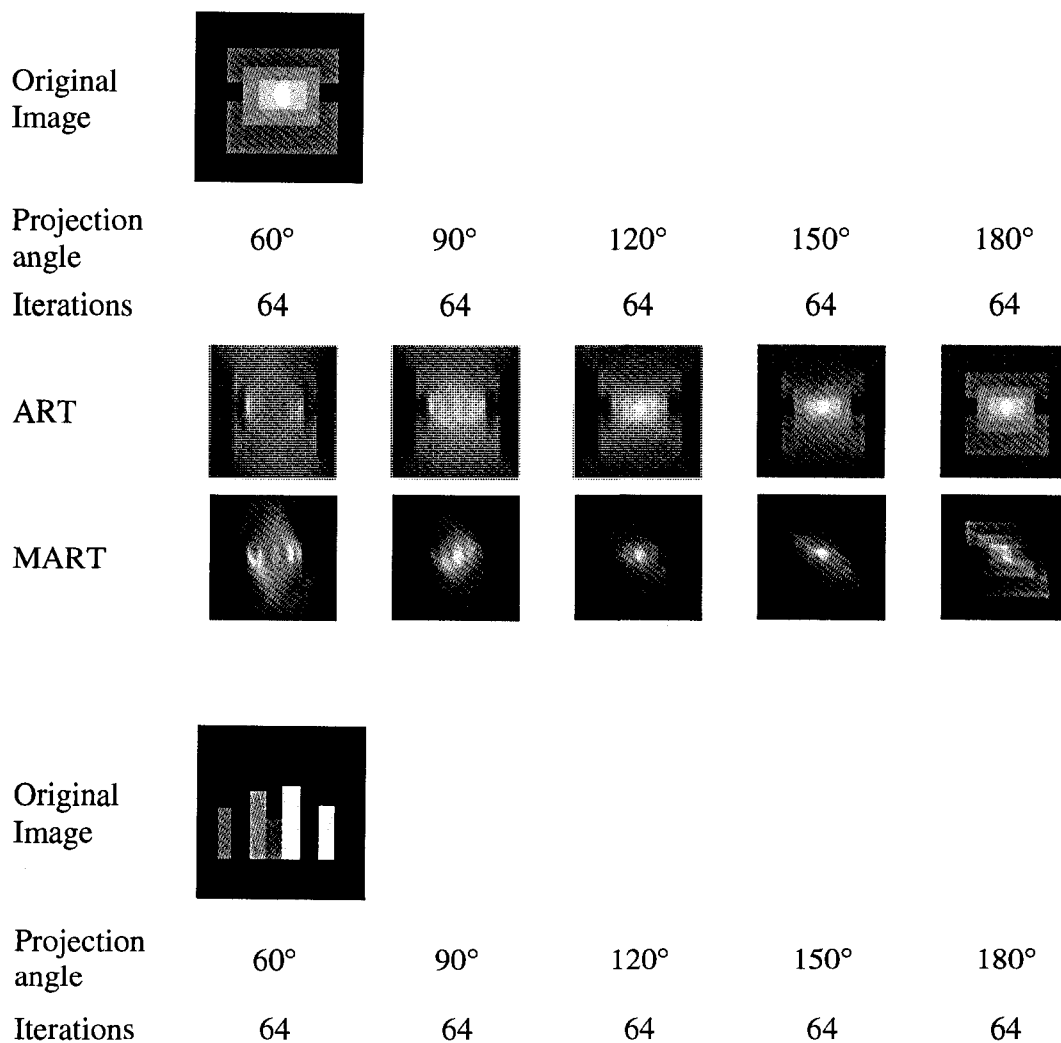


Figure 8: Image (volume slice) reconstruction results with parallel projection (a) original images (b) reconstructed images using binary sampling approximation (ray-cell intersection) (c) reconstructed images using binary sampling approximation (ray-cell distance) (d) reconstructed images using beam-pixel clipping

Figure 9 compares ART and MART with several projection angles. The format of the original image is 64×64 8-bit grayscale bitmap and our beam-pixel clipping was used for both reconstructions. Reconstructed images by MART are more likely to contain less noise than images by ART. Also, the MART method seems to converge sooner than the ART method. On the other hand, images by ART look more like the original. The MART seems to maximize the entropy while the additive ART seems to minimize the variance of the gray levels [15].



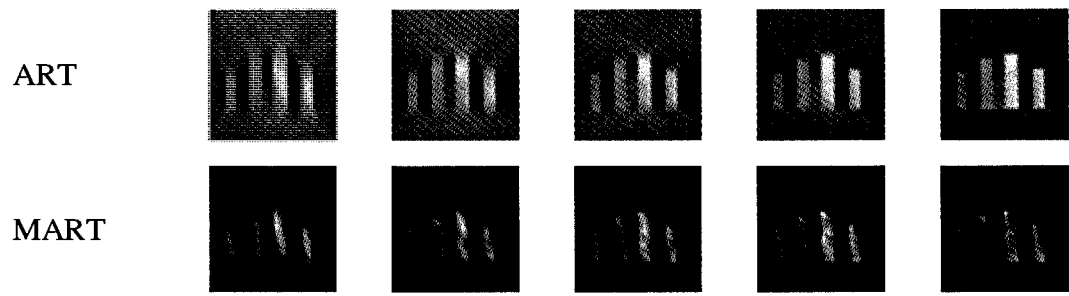


Figure 9: Image reconstruction results using ART and MART method with different projections

CHAPTER 4

SATELLITE-BASED 3D VOLUME RECONSTRUCTION

Satellite-borne and ground-based tomography and volume reconstruction using general optical instruments have more things to be taken into consideration than the previous image reconstruction with parallel projection. First of all, the projection is not parallel but perspective within the FOV of the optical instrument (i.e., fan beam projection). Second, due to perspective projection, weighting factor approximation of voxels is computationally more expensive. In this chapter, we discuss several different types of weighting factor approximations including beam tracing approximations as well as coordinate transformations between the satellite and the volume.

4.1 Constraints

In volume reconstruction using satellite-based measurement, several constraints need to be satisfied. These include the number of measured images, the resolution of the images, the focal point, and the projection angle in each orbital path. These factors play a crucial role in determining the resolution of the volume and the reconstruction performance. Most of all, a constraint that the target (aurora) is stationary during measurement should be assumed for volume reconstruction.

The resolution of reconstructed volumes depends on the number and the resolution of measured images. The maximum possible resolution can be calculated using

the product of the number of images, the image width and the image height. In real applications, images may contain some useless pixels that do not contribute to the volume region as shown in Figure 10. Those pixels (as ray-sums) cannot be used for any linear equation in algebraic reconstruction methods. There is also the so-called “stabilization regions” inside the volume region as shown in Figure 10. These regions lead to detail suppression since null or negative values occur in the iteration of algebraic methods [1]. Suppose the ratio of “real” pixels on average is R . The maximum volume resolution can be computed as follows:

$$V_x \cdot V_y \cdot V_z \leq N \cdot W \cdot H \cdot R \quad (9)$$

where N is the number of images, W is the width of the image, H is the height of the image, and V_x , V_y and V_z are the volume resolution on the x , y and z -axis. The ratio R is determined by FOV, focal point and distance between the instrument and the target zone. The satellite needs to keep an adequate distance from the target so that the ratio R is close to 1. If the satellite is too close to the target, it may fail to cover every area of the target zone. If it is too far from the target, the ratio decreases. As we show later, the best results occur where the satellite instrument is set to a target acquisition mode to fix a focal point to the center of the target.

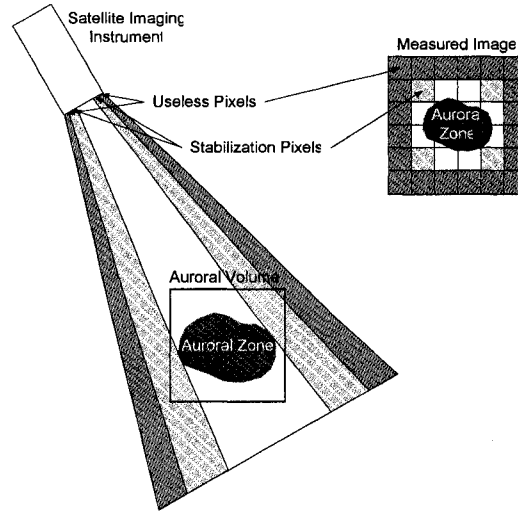


Figure 10: Unnecessary pixels during image measurement of auroral zone

To determine the quality of reconstructed volumes, the angular range of measurement is fairly important. According to [21], a minimum angle to achieve satisfactory results should be at least 50 - 70°. Although the wider angular range offers better reconstruction results in theory, there is a possibility that the target zone (aurora arcs and emission) is not stationary during measurement in a wider angular projection. In this case, a smaller projection angle may be better; it may produce more spatial noise, but will be subject to less temporal noise caused by the dynamic nature of the data. In this context, determining an appropriate angular range requires a complicated interaction between the degree of the target motion and the measuring time.

In optical tomography, the characteristics of the optical instrument affect the linear system in algebraic reconstruction methods. These include several parameters of camera lens, filter and CCD. In addition, atmospheric attenuation should be considered.

The matrix form of equation (1) is modified into:

$$R_n \approx C \sum_m W_{m(n)} X_{m(n)} \quad (10)$$

The constant attenuation is added via parameter C [11].

4.2 Coordinate transformations between optical instrument and volume

There are several major coordinate systems in use for positioning on the Earth. Geodetic Coordinate System with latitude ϕ and longitude λ is widely used for vehicles and any other equipment using Global Positioning System (GPS). In Space Physics and related studies, Geographic Coordinate System (GEO) and Geomagnetic Coordinate System (MAG) are in common use. GEO is based on the axis of the earth rotation while MAG is based on the earth's geomagnetic dipole axis. Some coordinate systems use spherical coordinates in terms of latitude, longitude and altitude while others use Cartesian coordinates in (x, y, z) . In order to reconstruct a volume, it is convenient to use its own coordinate system based on the origin of the volume in Cartesian coordinates. Therefore, no matter what kind of coordinate system is being used in satellites and ground-based observatories, coordinate system transformations are required between image projections measured from satellite instruments and ground-based observatories and volumes to be reconstructed. For detailed information regarding coordinate transformations, see [16].

In auroral volume tomography and volume reconstruction, all auroral images measured from a satellite optical instrument (auroral imager) include their coordinate information. These coordinates are acquired by an attitude control system or a star-sensor on the satellite. All coordinate systems of the measured images including GEO and Geodetic Coordinate System need to be converted into one of the Geocentric Coordinates in the Cartesian format as shown in Figure 11 (a). Once all coordinates are represented in Cartesian components in (x, y, z) , we need to define the position of a volume to be

reconstructed in GEO as shown in Figure 11 (b). The volume positioning and its own volume coordinate system (VOL) can be defined depending on the auroral mission. The conversion matrix from GEO to its own VOL, which is based on the volume's origin, can simply be obtained as shown in Figure 11 (c). Now all the coordinates of the images are represented in VOL, from which the volume can be reconstructed.

The volume's coordinates can then be transformed into another coordinate system such as GEO and MAG. For example, in most cases, the coordinates of reconstructed auroral volumes need to be transformed into MAG in order to look into the vertical profile of the auroral arcs and emissions. The diagram in Figure 12 shows the main process of the coordinate transformations in auroral volume reconstruction.

(a) Satellite measurement of auroral zone and coordinate information in GEO

(b) Target volume positioning in GEO

(c) Coordinate transformation from GEO to VOL and volume reconstruction in VOL

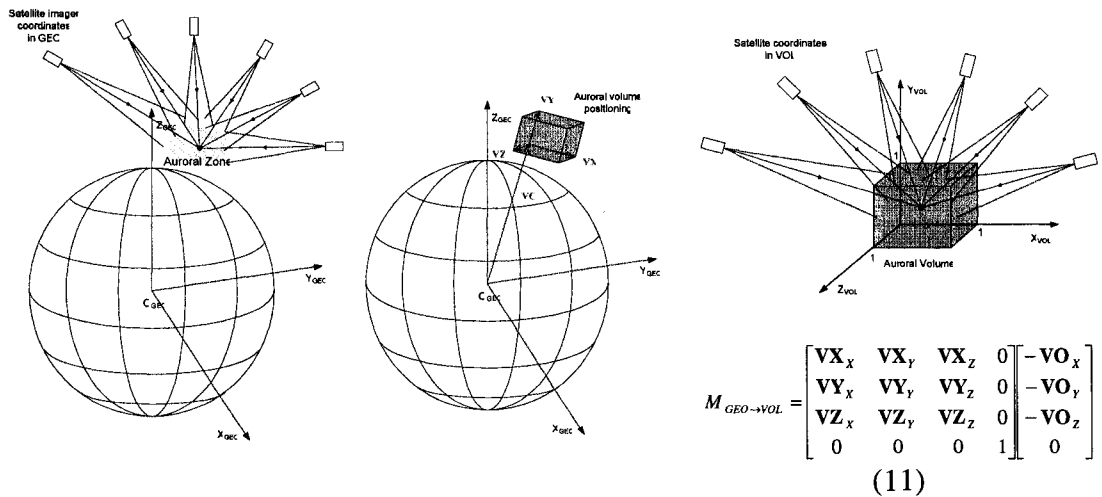


Figure 11: Coordinate transformation for satellite-based auroral volume reconstruction

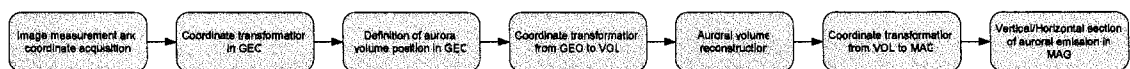


Figure 12: Main process of the coordinate transformations in auroral volume reconstruction

4.3 Beam tracing weighting factor approximations

Weighting factor approximation for volume reconstruction approximates the contribution ratio of each ray beam to each voxel. Conceptually it can be represented as the beam-clipped volume divided by the entire volume of each voxel. In order to obtain a more accurate weighting factor, which is close to the theoretical value, we discuss several beam tracing approximations. Conventional ray tracing approximations using each ray and each voxel's center can also be considered. These methods are relatively cheap, but there are several issues encountered (e.g., sampling) in terms of accuracy. Also, these methods are not appropriate when the projection is perspective, the resolution of the acquired images is relatively small, or each voxel of the volume is large.

Based on the previous image reconstruction with parallel projection, we suggest that the weighting factor approximation also plays a crucial role in volume reconstruction. We need to verify this hypothesis by developing and evaluating more accurate approximation techniques. Therefore we focus on different beam tracing approximations using beam-voxel clipping and beam-voxel sampling.

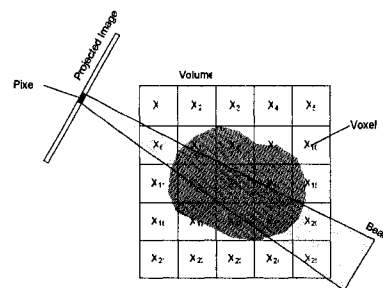


Figure 13: Beam tracing approximations in perspective projection

In beam tracing methods, each beam corresponding to each pixel of the projected image is represented as a long pyramidal volume. In a single projection, the beam volume's contribution ratio to each voxel of the volume is the weighting factor (for

perspective projection) as shown in Figure 13. Figure 14 (a) uses beam-voxel clipping. Every voxel is examined to see if there is an intersection or inclusion with the beam. If there is, then clipping between the beam and the voxel is performed and the clipped volume is calculated for its weighting factor. Although this method provides a more accurate weighting factor, it is somewhat more computationally complex. Figure 14 (b) shows a sampling approximation to the beam clipped ratio. We distribute sampling points in each voxel. The weighting factor of a voxel becomes the ratio of the number of samples included in the beam to the total number of samples in the voxel. When a rough volume reconstruction is good enough, such as in a preliminary analysis stage, we can use a binary sampling approximation (one sampling point) where the weighting factor is either 0 or 1. We can increase the number of samples when more accurate weighting factors are required.

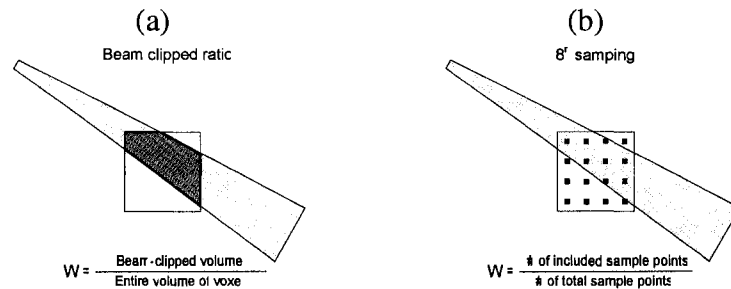


Figure 14: Two beam tracing approximations (a) Beam-voxel clipping (b) Beam-voxel sampling

We introduced two major ideas to compute weighting factors, each of which is applicable to some cases in terms of performance. When a more accurate volume reconstruction is required, we use beam-voxel clipping or beam-voxel sampling with many samples. On the other hand, beam-voxel sampling with a small number of samples requires less computation time. This trade-off raises a question of how accurate the weighting factor should be. Table 3 shows weighting factor results between two methods

using several random beam volumes. Beam-voxel sampling with one sample point has weighting factors that are either 0 or 1 (binary sampling); this is the most commonly used previous approach, but it may cause inaccurate volume reconstruction. The approximation results with 10^3 samples appears to be almost the same as the beam-voxel clipping results. But Table 3 doesn't explain how much the weighting factor affects the volume reconstruction result. We suggest that beam-voxel clipping has the best reconstruction performance and that there is an appropriate sample number in the sampling approximation in most cases, which is discussed with several volume results in Chapter 5.

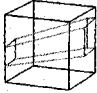
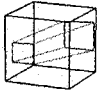
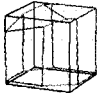
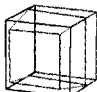
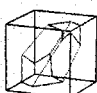
Test beam	Beam-voxel clipping method	Beam-voxel sampling			
		1^3 (binary)	2^3	4^3	10^3
	0.15798	1.0	0.125	0.21875	0.159
	0.14955	1.0	0.0	0.21875	0.152
	0.80775	1.0	1.0	0.84375	0.844
	0.85448	1.0	1.0	1.0	0.875
	0.26988	1.0	0.25	0.296875	0.27
Relative computation time on average	1	0.07	0.09	0.23	2.51

Table 3: Several weighting factor results between two methods

4.4 Optimizing approximations

The weighting factor approximations described above require costly computation in most cases. For instance, when the resolution of a volume to be reconstructed is 64^3 , each beam of the projection needs to be intersected with 64^3 voxels. In beam-voxel clipping, computation time to perform clipping increases as the number of intersected voxels increases. Even though such computation time is not a big issue in this volume reconstruction, it is better to optimize the approximation for better performance. In this sense, a tree-based voxel structure such as octree can be applied to the approximation. In the octree structure, the internal nodes have eight child nodes which are subdivided from the parent 3D box. For more detailed information, see [20].

In the implementation of optimizing the approximation described in this paper, such an octree structure is not used physically. Instead, we assume every voxel becomes one of the leaf nodes of an octree conceptually. In each projection to compute weighting factors, the beam is examined with the entire volume box to see if there is an intersection or inclusion. If the beam includes the volume box, all the weighting factors are equal to 1. If the beam has no intersection and no inclusion to the volume, all the factors are 0. Otherwise, the beam is examined with eight boxes subdivided from the volume box and the process is performed recursively. When this process goes down to one voxel, its weighting factor is determined by beam-voxel clipping or beam-voxel sampling.

4.5 Algorithm description

We now describe our algorithm for volume reconstruction using a set of images measured from an optical instrument. The optical instrument (e.g., auroral imager) has its own optical characteristics such as FOV and image resolution. The optics can have

distortion depending on the characteristics. For example, all-sky cameras with fish eye lens have extreme distortion. We don't discuss such cases but assume that the optics has no distortion.

The volume reconstruction process using algebraic reconstruction methods starts with an empty volume where all voxels have an initial value. Then the first image with its camera information is used for reconstruction. It produces a new perspective projection and each pixel of the image produces its own beam tracing projection. A set of weighting factors for the linear equation is computed through the beam tracing approximation. The approximation can use either beam-voxel clipping or beam-voxel sampling. The iteration of the reconstruction updates all voxels of the volume using the set of weighting factors. Then the iteration steps onto the next pixel of the image. Once the first image is completely used, a new perspective projection using the second image is performed. The entire process ends with the last image frame and all voxels of the volume are finalized.

As mentioned before, every pixel corresponds to a single iteration with the beam tracing approximation in order to compute weighting factors. Under the above assumption that there is no distortion in optics, each pixel's FOV is determined depending on the optical FOV and the resolution.

Our implementation consists of two functions as shown in Figure 15. The first function is volume rendering with a known volume in order to verify our algorithm. This volume rendering is also based on the beam tracing using perspective projection generated by a set of virtual cameras. The generated images in different projections are used for volume reconstruction using measured images. The measured images can be either images generated from volume rendering or images measured from satellite

instruments. Volume rendering is the exact reverse process of volume reconstruction; therefore we evaluate the effectiveness of our reconstruction algorithm using the known volume and the reconstructed volume.

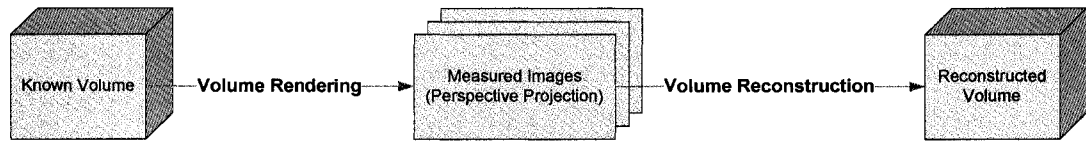


Figure 15: Verification of our algorithm using volume rendering and volume reconstruction

Since computing a set of weighting factors can be used for both volume rendering and volume reconstruction, the two functions are concurrently processed in our test application. In the test application, a volume with arbitrary voxel values and a set of virtual camera paths are generated. Using the camera paths, both volume rendering and volume reconstruction are performed. But the volume rendering process is omitted in real applications since measured images should exist in advance. The following is the pseudo code of the volume reconstruction process:

Create an empty volume

Initialize the volume with initial voxels (mostly 0's)

FOR *each measured image*

Load camera information of this projection (angle, position, FOV, etc)

Get the number of rays (pixels) of this projection

FOR *each pixel of this projection*

Get this ray-sum from pixel value

Create a beam

Compute all voxels' weighting factors

(using beam-voxel clipping or sampling)

Set a linear equation

Update the voxel values of the volume using one of algebraic methods

(ART, MART, etc)

ENDFOR *of each pixel*

ENDFOR *of each measured image*

4.6 Results

Our application as shown in Figure 16 is built on Java and OpenGL with JOGL (Java OpenGL). This implementation includes volume rendering along with volume reconstruction in order to verify our reconstruction algorithm. Both processes use the beam tracing projection to obtain more accuracy. This application starts with a known volume and the same sized empty volume with initial voxels. Once a set of virtual camera paths is specified, it is able to measure the known volume observed from a particular camera position, which generates a new camera view (camera projection). Each camera has its position information including camera, reference and up vector, along with the FOV and the resolution. The program then starts volume reconstruction using the known volume and the camera paths. A new measured image at a certain position is loaded according to the order of the camera paths. The measured image is used for volume reconstruction and then voxels of the empty volume are updated by the iteration. For weighting factor computation, the beam tracing will use, either beam-voxel clipping or beam-voxel sampling.

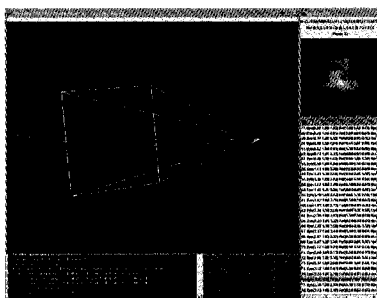


Figure 16: Our volume rendering and volume reconstruction application

Figure 17 shows 32^3 reconstructed volumes with a representative volume slice obtained using different weighting factor approximations. All cameras have 27° FOV with 64×64 image resolution. The number of projections is 80 and the angular range is

120°. The original column shaped volume represents simple auroral arcs. Columns (a), (b), and (c) are reconstructed volumes using beam-voxel sampling with different sampling points (1, 2³ and 4³). Row (1) uses a basic additive ART, row (2) uses SART, and row (3) uses MART.

Figure 18 shows a representative volume slice from reconstructed volumes in Figure 17 (1). Pixel (ray intensity) distributions on y=10, 11 and 12 are also given. As more sampling points are applied to beam-voxel sampling, the smoothness of volume slices increases, and it approaches that of volume slices using beam-voxel clipping.

Figure 19 is the same test as Figure 17 except for the resolution of the volumes (64³). Figure 20 is the same test as Figure 17 except the original volumes have gradient columns which is intended to represent simplified auroral arcs. Table 4 summarizes several volume reconstructions with different approximations, resolutions and volumes. Similarity of normalized voxels between the original volume and its reconstructed volume is given. The second similarity is a somewhat different figure-of-merit (FOM) function [13] defined as:

$$Similarity_2 = 1 - \frac{\sum \sqrt{(V_R - V_O)^2}}{\sum V_O} \quad (12)$$

where V_R and V_O are voxel values of the original and the reconstructed volume.

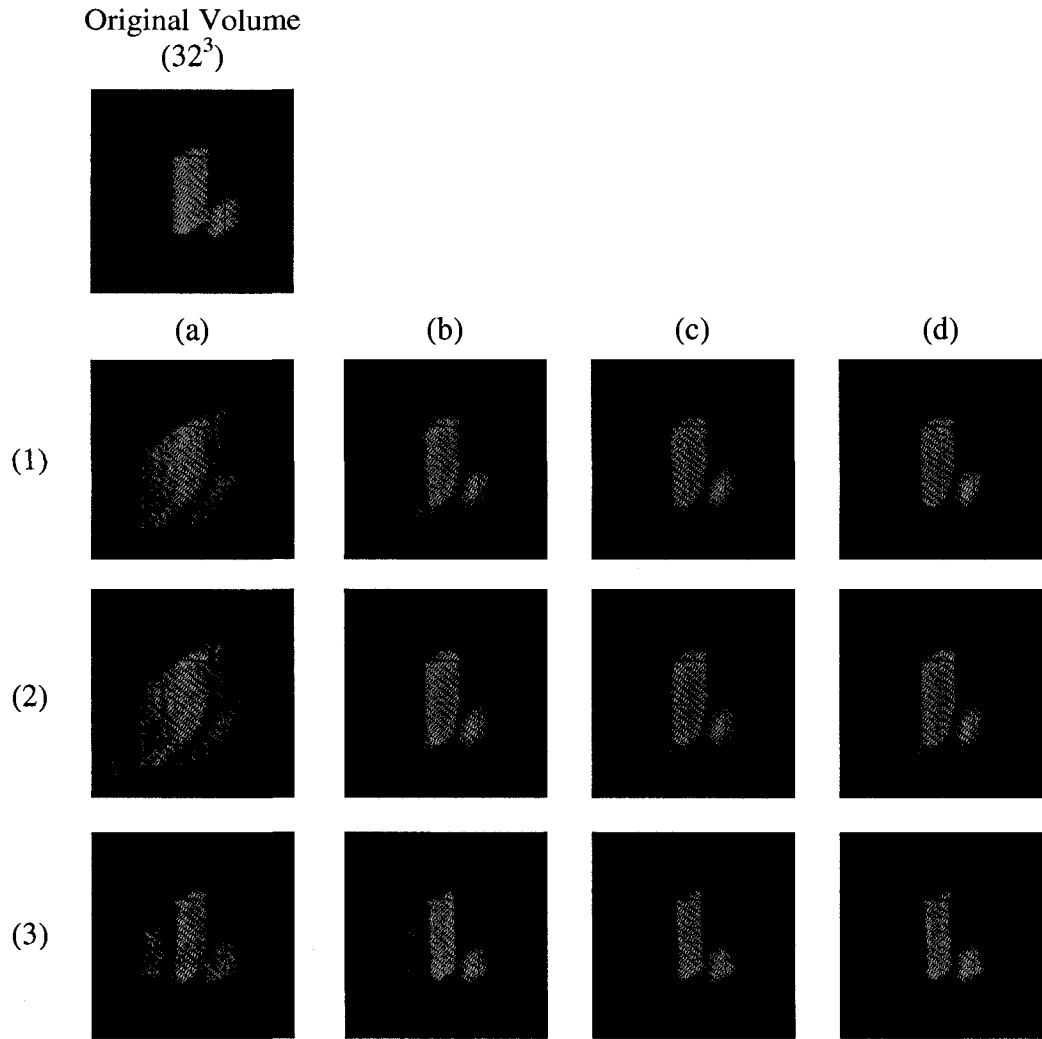


Figure 17: Different weighting factor approximation results of 32^3 volume (a) Beam-voxel sampling (binary) (b) Beam-voxel sampling (2^3) (c) Beam-voxel sampling (4^3) (d) Beam-voxel clipping

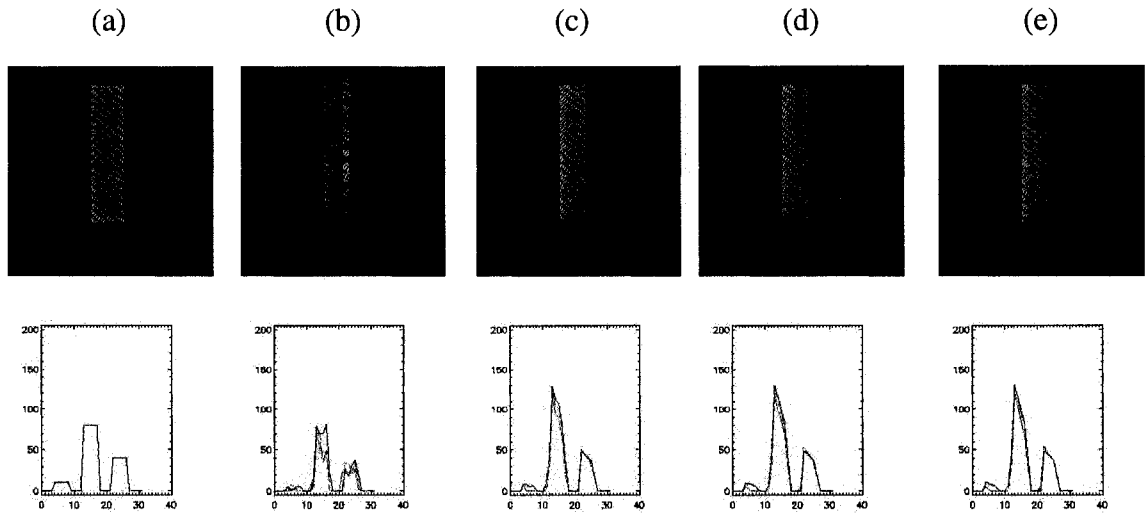


Figure 18: Representative volume slices ($z=16$) and pixel distributions ($y=10, 11, 12$) of Figure 17 (1) (a) Original volume (b) Beam-voxel sampling (binary) (c) Beam-voxel sampling (2^3) (d) Beam-voxel sampling (4^3) (e) Beam-voxel clipping

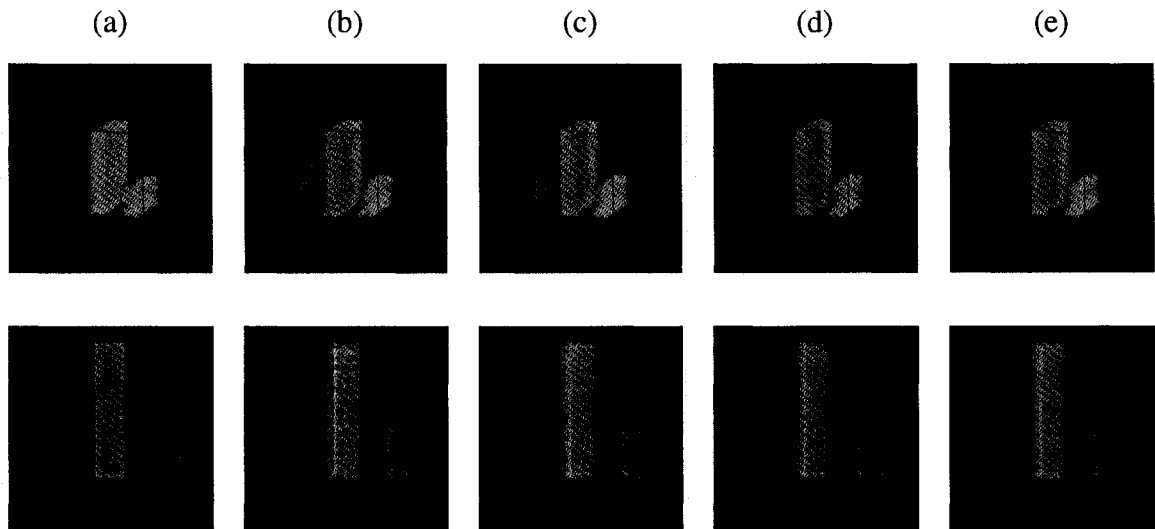


Figure 19: Different weighting factor approximation results and representative slices of 64^3 volume (a) Original volume (b) Beam-voxel sampling (binary) (c) Beam-voxel sampling (2^3) (d) Beam-voxel sampling (4^3) (e) Beam-voxel clipping

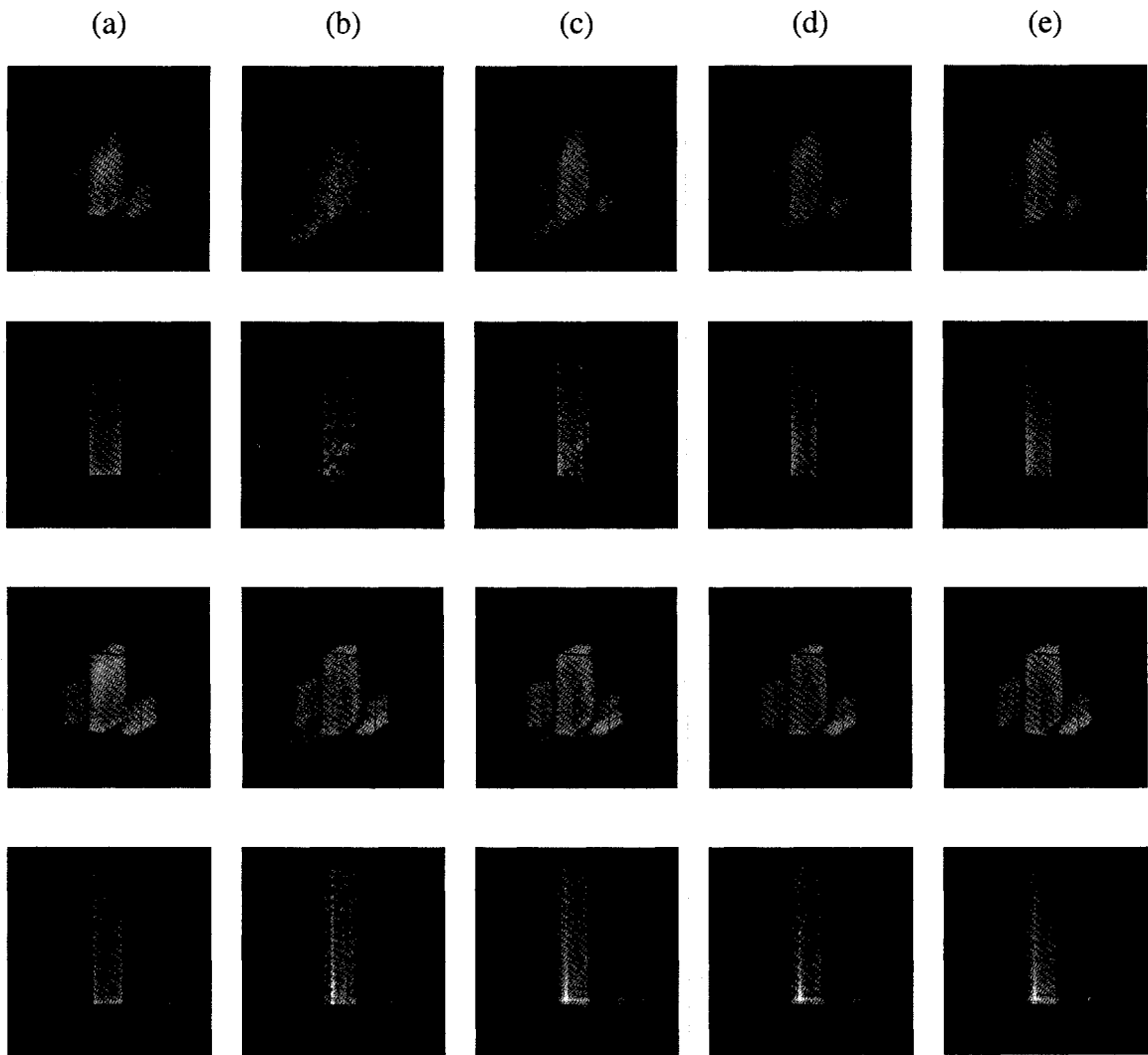


Figure 20: Different weighting factor approximation results and representative slices of gradient 32^3 and 64^3 volumes (a) Original volume (b) Beam-voxel sampling (binary) (c) Beam-voxel sampling (2^3) (d) Beam-voxel sampling (4^3) (e) Beam-voxel clipping

		Beam-voxel sampling (binary)	Beam-voxel sampling (2^3)	Beam-voxel sampling (4^3)	Beam-voxel Clipping
32 ³ volume #1	ART	0.36	0.56	0.58	0.58
		0.26	0.51	0.53	0.54
	MART	0.28 0.30	0.40 0.46	0.41 0.47	0.42 0.49
	SART	0.36 0.26	0.59 0.53	0.60 0.55	0.60 0.55
323 volume #2 (gradient)	ART	0.40 0.30	0.59 0.56	0.59 0.55	0.58 0.55
64 ³ volume #1	ART	0.30 0.26	0.40 0.36	0.40 0.37	0.40 0.37
	MART	0.18 0.20	0.21 0.25	0.22 0.26	0.22 0.26
643 volume #2	ART	0.53 0.47	0.61 0.58	0.62 0.60	0.62 0.59
	MART	0.25 0.28	0.30 0.34	0.30 0.35	0.32 0.37
64 ³ volume #3 (gradient)	ART	0.60 0.55	0.62 0.58	0.62 0.59	0.62 0.59

Table 4: Similarity and similarity2 of the original volume and the reconstructed volume using different approximations

The results as shown in Figure 17 through Figure 20 indicate that beam-voxel clipping produces more accurate volumes than beam-voxel sampling with a small number of sampling points. With a large number of sampling points (more than 4^3), the result approaches that of beam-voxel clipping. Two different beam tracing approximations provide a trade-off between the accuracy of reconstruction and computational complexity. In addition, the results show that ART and SART produce better looking data while MART produces less noise as discussed before by [15, 22].

In beam-voxel sampling, reconstruction of N^3 volume with 4^3 sampling points can be the same as reconstruction of $(4N)^3$ with 1 (binary) sampling point. But since reconstruction of a higher resolution volume requires more measured images (rays) for the linear system of algebraic reconstruction methods, a lower resolution volume

reconstruction with more sampling points is more proper when acquired images are not sufficient. We can also use beam-voxel clipping for accuracy in any case.

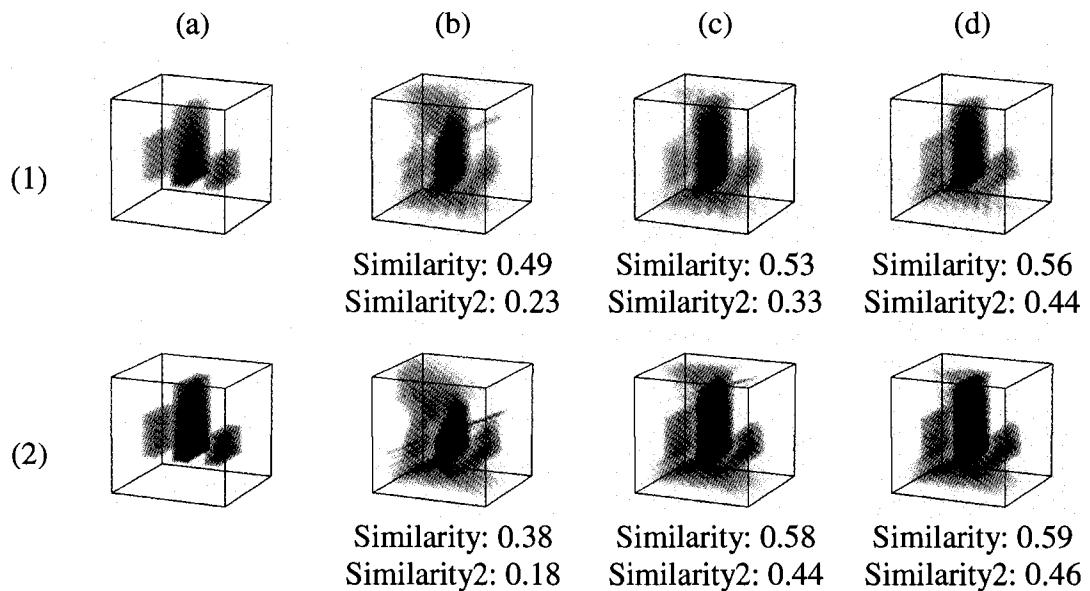


Figure 21: Reconstructed volumes and the similarity results using different focal points (a) Original volume (b) Reconstructed volumes with a focal point outer of the volume (-0.5) (c) Reconstructed volumes with a focal point near bottom (0.0) (d) Reconstructed volumes with a focal point in the volume center (0.5)

Since e-POP allows changing the focal point, we need to understand the effect on our algorithm. Although, there are many conditions to be considered such as the direction of the orbit, the position of the target zone, and the distance between the target and the instrument, we simply performed three experiments with a different focal point.

Figure 21 shows several reconstructed volumes to evaluate different focal points, along with two similarity results. Figure 21 (a) are the original volumes, and Figure 21 (b), (c) and (d) are the reconstructed volume with different focal points. Suppose the volume coordinates are (0, 0, 0) and (1, 1, 1). Figure 21 (b) shows the reconstructed volume using a focal point below the volume (0.5, -0.5, 0.5). Figure 21 (c) uses a focal point at the bottom center of the volume (0.5, 0, 0.5) and Figure 21 (d) has a focal point of the center of the volume (0.5, 0.5, 0.5). Figure 21 (1) and Figure 21 (2) have different

orbital paths. Although these results use extreme orbital paths, it indicates why satellite instruments need to fix a focal point in or near the center of the target volume under the target acquisition mode, as described in chapter 4.1. In the case of Figure 21 (b), the satellite fails to cover every area of the target zone, which can cause incomplete solutions of algebraic reconstruction methods.

4.7 Conclusion

We have developed a tomographic volume reconstruction algorithm designed to use measured images from satellite-borne optical instruments. Our scheme can be used for reconstructing auroral volumes to observe the internal structure (e.g., vertical profile of intensity) of auroral arcs, which is not yet clearly known. On-board auroral imaging instruments (auroral imager) of the e-POP satellite will take a set of auroral pictures, which are used for auroral volume reconstruction. Auroral measurement will be performed under a target acquisition mode in which the instrument will have a fixed focal point in or near the target auroral zone. Depending on the number and the resolution of images taken in each orbital path, the resolution of reconstructed volumes is determined.

Our volume reconstruction is based on algebraic reconstruction methods, which are iterative methods that converge to a solution as the iteration proceeds. Algebraic methods such as ART and MART have advantages where the angular range of projection is small and there are not enough computation resources, which satisfies our constraint that the angle of satellite-based auroral measurement is usually much less than 180° . In each ray-projection of algebraic reconstruction methods, a set of weighting factors as coefficients of the linear equation is required. We have shown that weighting factor approximation plays a crucial role in the quality of reconstructed results. Our

approximation employs beam tracing techniques in which each ray is regarded as a long pyramidal beam. Our beam-voxel clipping makes it possible to obtain more accurate weighting factors, which improves the quality of reconstructed results. In some cases where we do not need high quality of reconstructed volumes, beam-voxel sampling with fewer sampling points can be applied to the reconstruction solution in order to achieve faster performance.

The volume reconstruction process starts with a set of initial voxel values and continues until all images acquired in a single orbital path are used. Beam tracing projection to compute a set of weighting factors is performed for each pixel of every measured image. For this projection, the image's coordinate information, including its target position, instrument position, and instrument roll information, is used along with the optical characteristics of the satellite instrument such as FOV and image resolution. Whenever a set of weighting factors is computed, the iterative method updates the voxel values using the factors and the sum of ray intensity (measured pixel value). Once all images are used for reconstructing the volume, the iteration ends with a set of voxel values that converge to the solution of its linear system.

We have performed reconstruction tests to evaluate our algorithm. Simultaneously, we have also implemented volume rendering which is the reverse process of volume reconstruction to verify our algorithm. Beam-voxel clipping produces more accurate results than beam-voxel sampling with a small number of samplings. Beam-voxel sampling with a large number of samplings performs nearly as well as beam-voxel clipping. Both methods can cause costly computational time and resources. Depending on

the purpose of the reconstruction, different beam-tracing based approximations can be used.

CHAPTER 5

ADAPTIVE TIME-VARYING VOLUME RECONSTRUCTION

5.1 Motivation

In the previous chapter, we have developed a 3D auroral volume reconstruction algorithm using tomographic imaging techniques based on algebraic methods. This scheme assumes that the source object (aurora) is stationary or moving extremely slowly during image projection in order to maximize the quality of reconstructed volumes. Unfortunately, in most cases, auroral arcs drift at various rates and auroral emissions change in shape. Even stationary aurora can change shape over time. In this chapter, we focus on a suitable scheme to reconstruct time-varying auroral volumes using a set of sequential auroral images measured from satellite-borne imaging instruments. This is similar to the multi auroral volume reconstruction using previous results discussed by [11]. Unlike their method, our scheme produces a time-series of auroral volumes using sequential auroral images from a single satellite instrument, adapting the auroral motion in a period. We also evaluate our algorithm on non-stationary auroral volumes to validate the effects of motion on the simulation.

According to [7], auroral motions can be classified as global-scale motions, large-scale motions and small-scale motions. In some cases, motions and changes such as

fluctuations may also take place very rapidly. The speed of the global-scale auroral motions is less than a kilometer per second. Small-scale motions such as the motion of rays along auroral forms are somewhat faster (approximately tens of kilometers per second). More generally, the speed can vary from being nearly stationary to several 10's of km/s, depending on the type of aurora.

The orbit of the e-POP satellite will be at several hundred kilometers altitude on average (a nominal perigee of 315 km and an apogee of 1500 km) and the optical instrument (FAI imager) will have an effective spatial resolution of several kilometers. The FAI-SV will provide coverage of 380×380 km at 1000 km altitude, while the FAI-SI will provide coverage of 430×430 km [27]. Therefore the auroral motions usually seem to have little influence on the measurement of a single auroral image. However, multiple auroral images measured over a long period cannot be used for reconstruction if the speed is fast.

5.2 Auroral measurement

For time-varying auroral volume reconstruction, we need a set of sequential auroral images, all of which point to a fixed or limited focal target of an auroral zone as shown in Figure 22. In satellite missions for auroral measurement, the auroral imaging instrument will be set to a target acquisition mode. In the target acquisition mode in each orbital path, the instrument will point to a limited auroral zone. The volume area to be reconstructed should cover all auroral arcs and their motions as shown in Figure 22. In e-POP mission, it will take approximately from 2 to 15 minutes to acquire a set of images in a single path, depending on the precise altitude of the satellite [27].

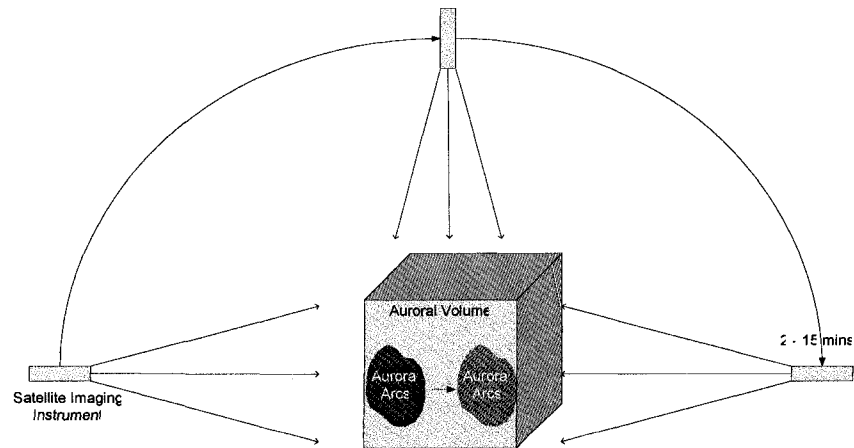


Figure 22: Time-varying auroral motion and satellite measurement

As mentioned before, in auroral measurement using satellite imaging instruments, several constraints must be satisfied including the number and resolution of measured images, and the focal point and angular range of measurements in the orbital path. These factors determine the resolution and the quality of reconstructed volumes. Each reconstructed volume is generated using a sequence of images from a single orbital path. After auroral image acquisition, we need to define an auroral zone (auroral volume) in the satellite's coordinate system. The volume zone should cover all auroral emissions and their motions, which means there is no significant light intensity outside the volume. Rectangular shaped volume is usual, but not necessary. Variable voxel size is also possible depending on the distribution of the target. For instance, we can apply higher resolution to the vicinity of the auroral arcs.

5.3 Method

Our previous volume reconstruction assumes auroras are stationary or slow-moving, and auroral emissions have little fluctuation during measurement. When aurora arcs drift or change rapidly, the previous scheme is not appropriate. We introduce a time-

varying volume reconstruction algorithm using time-varying consecutive auroral images from a single orbital path. When enough images for single volume reconstruction are acquired, a proper minimum projection angle is the only constraint to be considered for volume reconstruction. This sequence defines a minimum projection angle as shown in Figure 23. This angle represents a compromise. In theory, a wide angular range offers better reconstruction results. But there is a possibility that the target zone (aurora arcs and emission) is not stationary during measurement in such wide projections. In this case, a lower projection angle would be more appropriate. This trade-off raises a question of how much an appropriate angular range is. According to [21], it is possible to obtain a reasonable result where the angular ranges of the projections are $50 - 70^\circ$ through algebraic reconstruction methods. In our application, there is no absolute answer since the reconstruction performance varies depending on the auroral motion and the measuring time. We explore a minimum projection angle to achieve acceptable auroral volumes reconstruction.

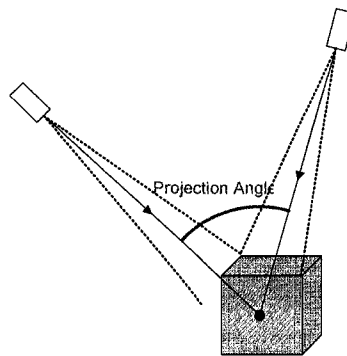


Figure 23: Minimum projection (measurement) angle

As shown in Figure 24, the scheme starts to reconstruct a volume using some consecutive images where auroras are regarded as “almost stationary”. The image set used for each reconstruction should satisfy the minimum angular range of projection.

Once the first volume reconstruction is completed, the next volume is reconstructed using the next sequential images. These images are overlapped between two sequential volumes. For example, as shown in Figure 24, the first volume reconstruction uses the images from frame 1 to frame 7, the second volume reconstruction from frame 2 to frame 8, and so on. The time stamp of each volume is equal to the average time of measured images used for reconstructing the volume in order to represent the middle of the actual motion of the volume.

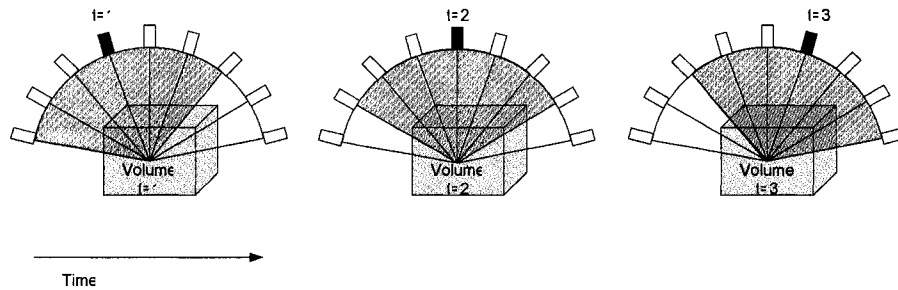


Figure 24: Time-varying multi-volume reconstruction in a single orbital path

The number of volumes available for reconstruction is determined by the number of acquired images and the projection angle. As the angular range decreases, more reconstructed volumes can be obtained. Since reconstructed volumes are low in quality using such small projection angles, it offers another trade-off. Therefore we need to consider the number of time-varying volumes as well as the projection angle, along with the motion of the source. Because sufficient images from FAI-SI will be acquired in each orbital path, a large number of volumes can be generated from a limited range of projections. In some cases, almost hundreds of 64^3 time-series volumes are expected to be generated using this scheme.

In this volume reconstruction with algebraic reconstruction methods start with a set of initial guesses for unknown voxel values.

A prior knowledge for the voxel values can be incorporated into the reconstruction methods [21, 25]. A better guess can make the reconstruction converge to the solution faster, which may affect the quality or the characteristics (e.g., contrast) of reconstructed volumes. Such a method to make use of a prior knowledge for the reconstruction method was attempted by [11]. Auroral images measured from several ground-based cameras were regarded as a time-sequence of a moving object. The shifted values of the first result were used as a first estimate for all other reconstruction. Therefore in the reconstruction procedure, a volume's initial values can be set to the previous volume's final values for fast convergence as shown in Figure 25. If such a motion (shifting) knowledge is not available, the reconstructed result can be worse.

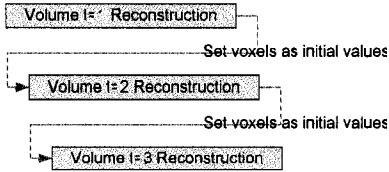


Figure 25: The voxels of the previous reconstructed volume as initial guesses for the next reconstruction

For this method, the motion of auroras should be defined through the prior analysis and other measurements. The degree of auroral motion determines the number of images available and the angular range. Since the number of images determines the number of iterations of algebraic methods, it affects the maximum resolution of reconstructed volumes. If the angle is less than the minimum required angle (e.g., 60°), it is not appropriate to proceed on the reconstruction process. Otherwise, the resolution of volumes to be reconstructed is determined. Depending on the number of available images and angle, time-varying volume reconstruction is performed. Figure 26 describes the major steps of this scheme.

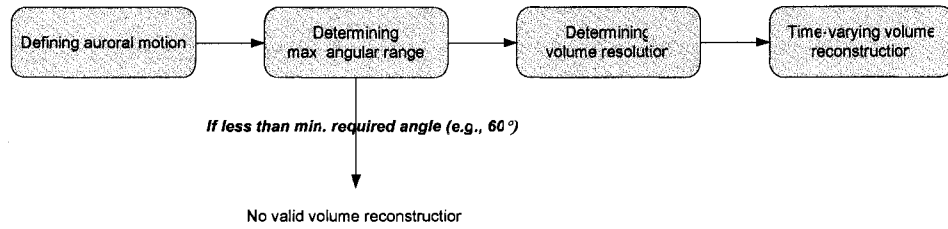


Figure 26: Preprocess of time-varying auroral volume reconstruction

5.4 Results

Figure 27 shows 64^3 reconstructed volumes using different projection angles with the basic additive ART. All cameras have 27° FOV with 64×64 image resolution. The number of iterations is 100. Table 5 summarizes the similarity between the original and the reconstructed volumes. The similarity increases as the angular range increase. Although it doesn't offer a firm answer about what the suitable angle for projection should be, the quality of reconstructed volumes fairly improves when the projection angle becomes around 100° - 120° . However 60° projection still produces a reasonable result.

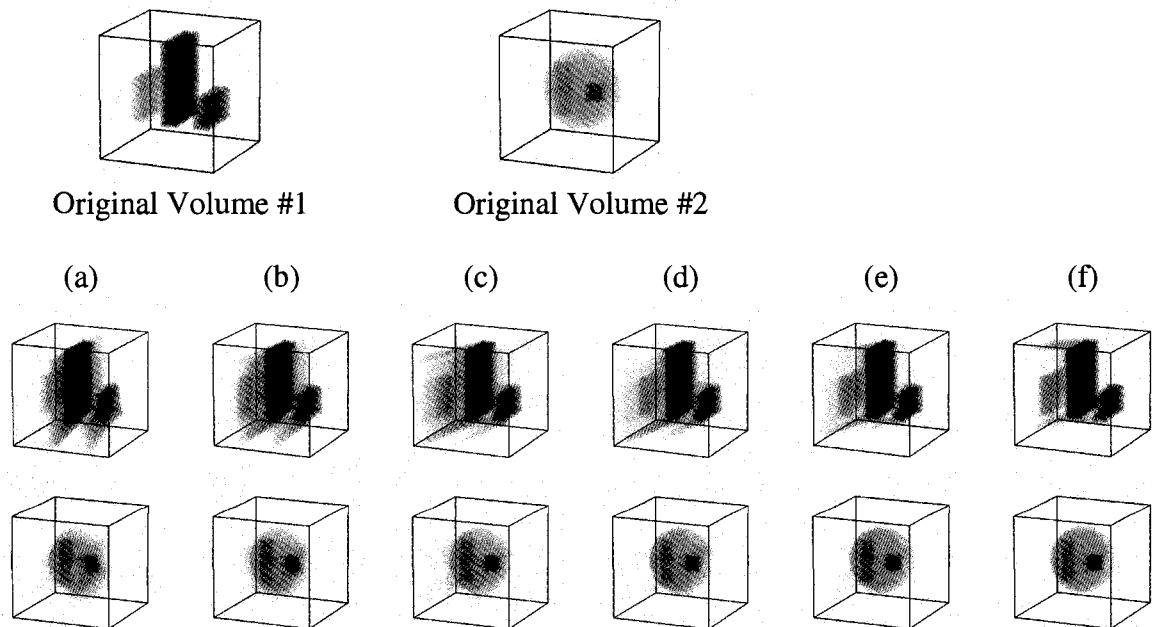


Figure 27: Original and reconstructed 64^3 volumes using ART with different projection angles (a) 60° (b) 80° (c) 100° (d) 120° (e) 140° (f) 160°

	60°	80°	100°	120°	140°	160°
Volume #1	0.51	0.56	0.57	0.62	0.62	0.62
Volume #2	0.20	0.26	0.31	0.37	0.40	0.43

Table 5: Similarity between the original and reconstructed volumes above

In order to test our time-varying volume reconstruction, we simulated the motion of auroral arcs that move at the speed of approximately 0.1 km/s as shown in Figure 28. We assume that the satellite instrument for the auroral measurement takes sufficient auroral images for 15 minutes (maximum apogee) in an orbital path. The angular range of projection (measurement) is 180°, similar to Figure 22. The size of the volume to be reconstructed is 300 km × 300 km × 300 km and the resolution of the volume is 64³. The only constraints to be considered are the motion of the auroras and the projection angle. Figure 29 shows several reconstructed volumes with different projection angles (180°, 120°, 100°, 80° and 60°) at different time stamps (300, 350, 400, 450, 500 and 550 sec). Since there is only a single volume available using 180° projection angle, any volume at other time stamps is not applicable as shown in Figure 29 (2). On the other hand, in the case of volume reconstructions with 120° projection angle, reconstructed volumes available are from 300 sec to 600 sec. For the same reason, reconstructed volumes available with 60° projection angle are from 150 sec to 750 sec.

Table 6 summarizes the similarity between the original and the reconstructed volumes at a certain time. Generally, reconstructed volumes with a small projection angle tend to be more similar to the original volumes at the corresponding time. This result shows that our time-varying volume reconstruction scheme enables the reconstruction method to be adaptive to the motion of the original volume. Reconstruction experiments when auroral motion opposite to satellite motion produced similar results.

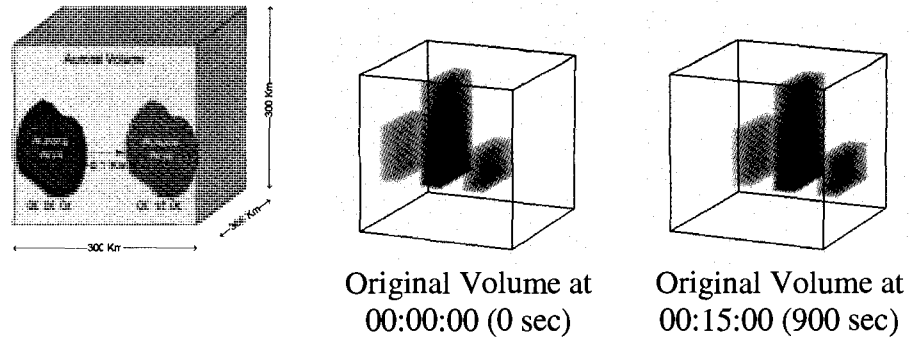


Figure 28: Time-varying volume reconstruction test

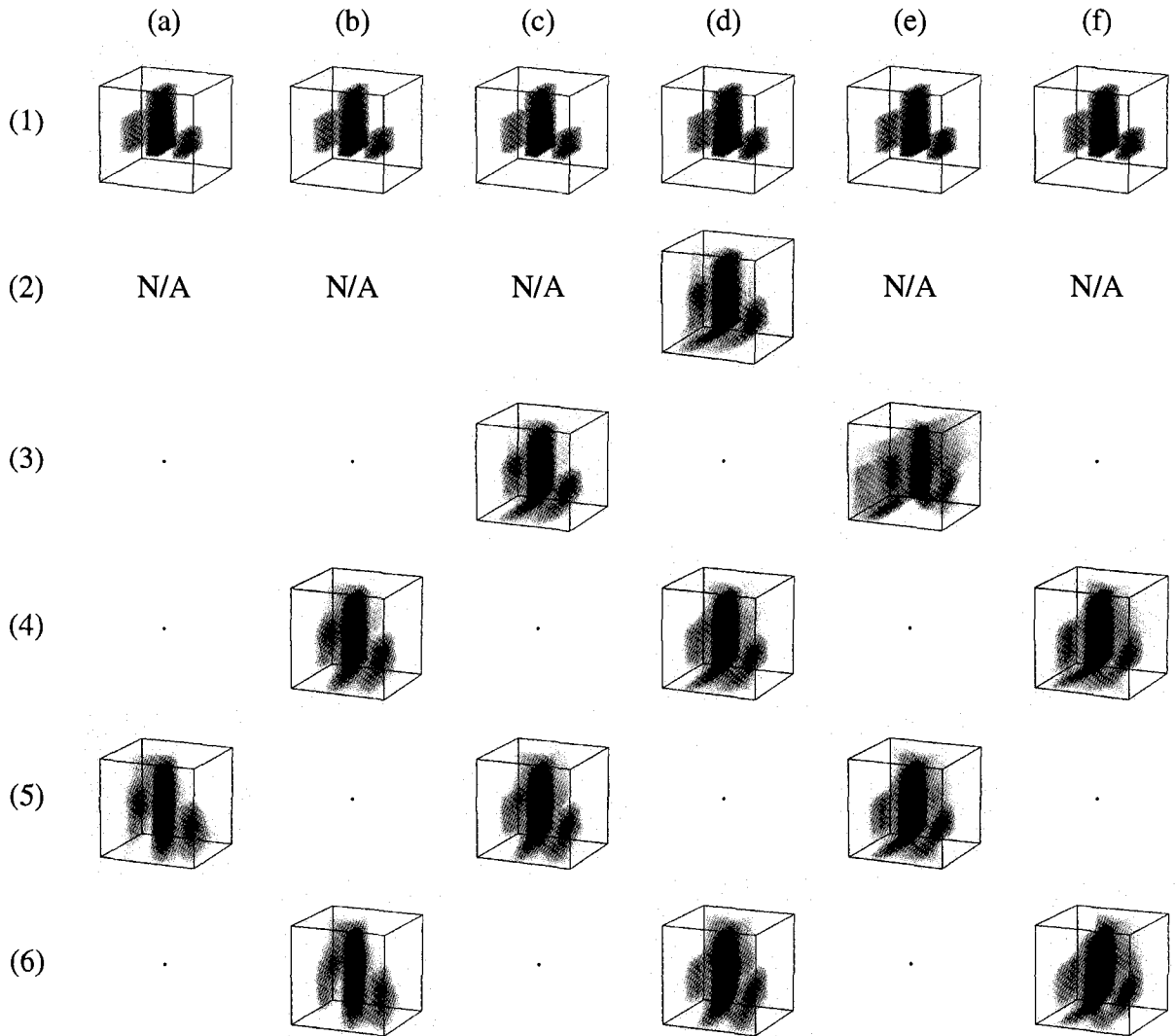


Figure 29: Time-varying reconstructed volumes using ART (a) 00:05:00 (300 sec) (b) 00:05:50 (350 sec) (c) 00:06:40 (400 sec) (d) 00:07:30 (450 sec) (e) 00:08:20 (500 sec) (f) 00:09:10 (550 sec) (1) Original volumes (2) A reconstructed volume with 180° projection angle (3) Reconstructed volumes with 120° projection angle (4) Reconstructed volumes with 100° projection angle (5) Reconstructed volumes with 80° projection angle (6) Reconstructed volumes with 60° projection angle

Time	Position	Projection Angle				
		180°	120°	100°	80°	60°
0 sec	0°	-0.30
50 sec	10°	-0.30
100 sec	20°	-0.25
150 sec	30°	-0.17
200 sec	40°	-0.08
250 sec	50°	0.01	.	.	.	0.08
300 sec	60°	0.10	.	.	0.19	.
350 sec	70°	0.20	.	0.24	.	0.26 (0.25)
400 sec	80°	0.29	0.32	.	0.34 (0.26)	.
450 sec	90°	0.39	.	0.44 (0.19)	.	0.45 (0.40)
500 sec	100°	0.47	0.25 (0.25)	.	0.55 (0.37)	.
550 sec	110°	0.41	.	0.48 (0.32)	.	0.52 (0.48)
600 sec	120°	0.26	.	.	0.34 (0.27)	.
650 sec	130°	0.13	.	.	.	0.28 (0.28)
700 sec	140°	0.03
750 sec	150°	-0.07
800 sec	160°	-0.15
850 sec	170°	-0.22
900 sec	180°	-0.28

Table 6: Similarity changes between time-varying original and reconstructed volumes using ART

Figure 30 shows different time-varying volume reconstruction results, along with a representative volume slice ($z=2$). While the motion of the source moves slowly in the previous reconstruction, the speed of this source is much faster. In addition, the direction of the motion is perpendicular to the orbital plane of the measurement (image projection). The measurement takes 3 minutes (around perigee) to acquire a sequence of images with an angular range of 180° . The resolution of the reconstructed volumes is 32^3 . We also assume that the number of measured images is sufficient for each reconstruction procedure. Therefore the only constraints to be considered are the motion of the auroras and the projection angle. Table 7 summarizes the similarity between the original and the reconstructed volumes at a certain time. Similar to the previous result, it also indicates

that reconstructed volumes with a small projection angle (60° , 80°) adapt to the motion of the original volume.

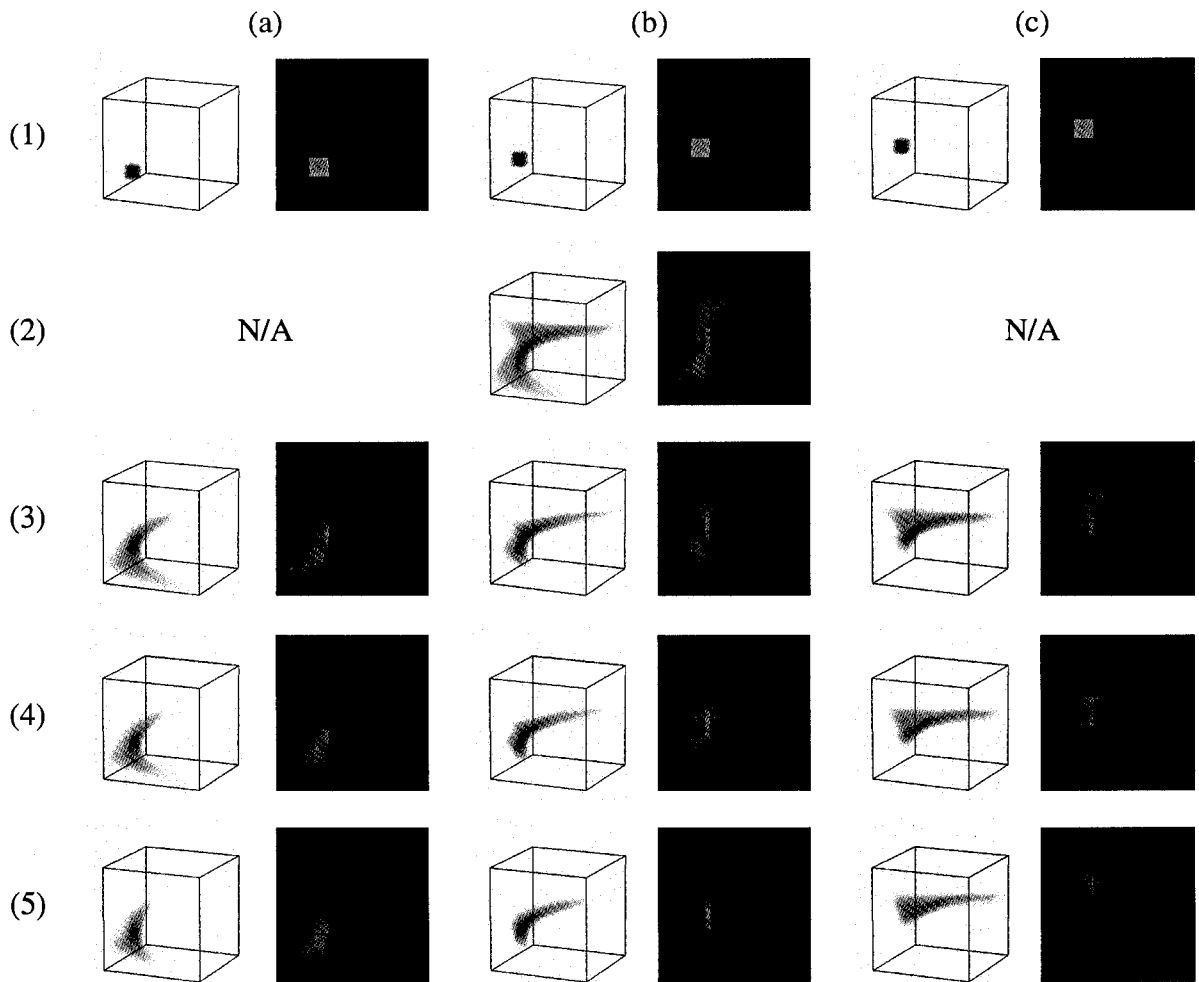


Figure 30: Original and reconstructed volumes with a representative volume slice ($z=2$)
 (a) Volumes at 50 sec (b) Volumes at 90 sec (c) Volumes at 130 sec (1) Original volumes (2) A reconstructed volume with 180° projection angle (3) Reconstructed volumes with 100° projection angle (4) Reconstructed volumes with 80° projection angle (5) Reconstructed volumes with 60° projection angle

Time	Position	Projection Angle			
		180°	100°	80°	60°
50 sec	50°	-0.41	-0.18	-0.05	0.12
90 sec	90°	-0.50	-0.07	0.07	0.20
130 sec	130°	-0.51	-0.15	0.00	-0.03

Table 7: Similarity changes between time-varying original and reconstructed volumes using ART

5.5 Conclusion and future work

In satellite-based auroral measurement, the optical imaging instrument will have a fixed focal point relative to the target auroral zone to take a set of sequential images. It will take approximately from 2 to 15 minutes to take a set of images in a single orbital path of the e-POP satellite. During that time, auroras can move far enough during the image acquisition that regular volume reconstruction methods may not be satisfactory. Our time-varying volume reconstruction scheme addresses this case, reconstructing time-varying volumes that adapt to the motion of auroras. This scheme performs multi volume reconstruction processes using some sequential images measured within a small projection angle where auroras are considered “almost stationary”. The images used for each volume reconstruction are overlapped. The time of each reconstructed volume becomes the average time of images used for the reconstruction procedure.

As shown in Figure 27, the angular range of projection (measurement) has influence on the quality of reconstruction. Although a wider projection angle (100-120°) achieves more accurate results, a small projection angle (60°) still offers acceptable results and is less sensitive to motion. We have implemented the time-varying reconstruction scheme to evaluate our algorithm using measured images of known volumes that move over time. From the results, reconstructed volumes with a small projection angle are more likely to be similar to the original volumes at the corresponding time. However, an adequate projection angle varies, depending on conditions that include the number of measured images, the target motion, and the precise orbital direction of the satellite.

We need to perform more experimentation with different speeds, directions, and shape changing to better identify conditions for which our algorithm is useful. When auroras move too fast during measuring within such a small projection angle, this reconstruction scheme is not appropriate. If the motion of the volume is predictable, we can shift or resize the volume so that each voxel (ray intensity) adapts to the motion, a suggestion made by [11] in the context of ground-based auroral tomography. Figure 31 describes the idea of time-varying reconstruction along with adaptive volume positioning.

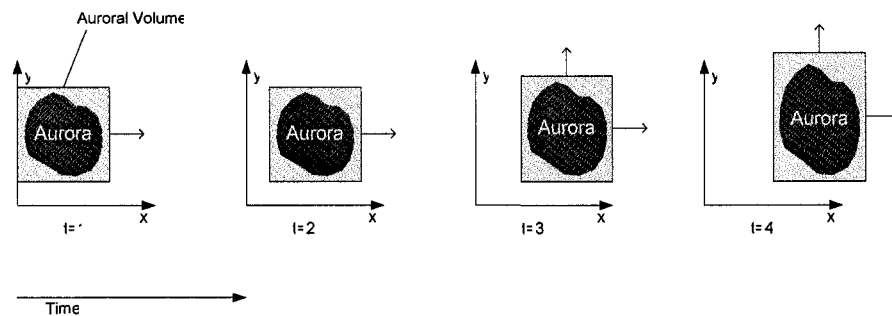


Figure 31: Time-varying adaptive volume positioning

In addition, we can apply parallel computing to this time-varying reconstruction method since volume reconstruction requires costly computational time and system resources. This solution can reconstruct multiple volumes simultaneously as shown in Figure 32. Each process performs sequential volume reconstructions where some image projections are overlapped. Weighting factor computation of the overlapped measured image can be cached for better performance.

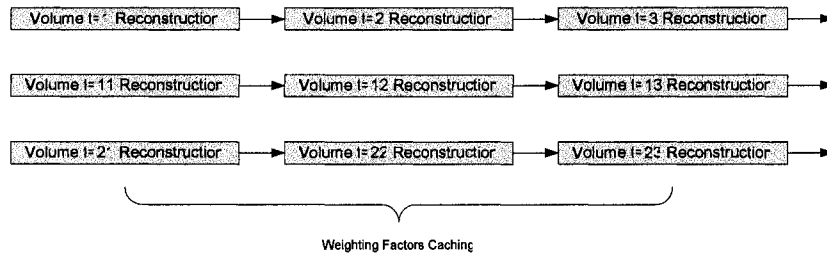


Figure 32: Parallel time-varying volume reconstruction

LIST OF REFERENCES

- [1] Alpatov, V. V., Pickalov, V.V., Lihachov, A.V., Informational analysis of auroral tomography, Auroral Tomography Workshop Proceedings, IRF Scientific Report 213, 35-45, August, 1993
- [2] Ammeraal, L., Computer Graphics for Java Programmers, First Edition, John Wiley & Sons, 1998
- [3] Angel, E., Interactive Computer Graphics, A Top-down Approach Using OpenGL, Fourth Edition Addison Wesley, 2005
- [4] Aso, T., Ejiri, M., Urashima, A., Miyaoka, H., Steen, A., Brandstrom, U., Gustavsson, B., First results of auroral tomography from ALIS-Japan multi-station observations in March, 1995, Earth Planets Space, 50, 81-86, 1998
- [5] Aso, T., Muguruma, K., Yabu, T., Hashimoto, H., Abe, M., Ejiri, M., A Note on the Computed Auroral Tomography by the MART method, Auroral Tomography Workshop Proceedings, IRF Scientific Report 213, 23-34, August, 1993
- [6] Atkinson, C. H., Soria, J., Algebraic Reconstruction Techniques for Tomographic Particle Image Velocimetry, 16th Australasian Fluid Mechanics Conference, Crown Plaza, Gold Coast, Australia, December 2-7, 2007
- [7] Davis, N., The Aurora Watcher's Handbook, University of Alaska Press, 1992
- [8] Davydov, V. S., Pivovarov, V. V., Some results of 3D aurora reconstruction based on single TV images and height profiles of brightness, Geomagnetism and Aeronomy, Vol. 34, No. 5, April, 1995
- [9] Davydov, V.S., Pivovarov, V.V., Test of auroral tomography methods for the ALIS project, Auroral Tomography Workshop Proceedings, IRF Scientific Report 213, 23-34, August, 1993
- [10] Donaire, J. G., Ortigosa, P. M., Garcia, I., Evaluation of the performance of a MART algorithm using blobs, Proc. IASTED International Conference on Signal and Image Processing, 1998

- [11] Frey, H. U., Frey, S., Lanchester, B. S., Kosch, M., Optical tomography of the aurora and EISCAT, *Ann. Geophysicae* 16, 1332-1342, 1998a, © EGS – Springer-Verlag
- [12] Frey, H. U., Frey, S., Larson, D., Nygren, T., Semeter, J., Tomographic methods for magnetospheric applications, "Science closure and enabling technologies for constellation class missions", eds. Angelopoulos, V., Panetta, P., University of California, 72-77, 1998b
- [13] Fu, X., Herman, G. T., Carvalho, B. M., Liao, H. Y., Optimized algebraic reconstruction technique for generation of grain maps based on three-dimensional x-ray diffraction (3DXRD), *Optical Engineering*, 45(11), 116501, November, 2006
- [14] Funkhouser, T., Carlbom, I., Elko, G., Pingali, G., Sondhi, M., West, J., A beam tracing approach to acoustics modeling for interactive virtual environments, *Proceedings of the 25th annual conference on Computer graphics and interactive techniques (SIGGRAPH'98)*, 21-32, 1998
- [15] Gordon, R., Bender, R., Herman, G. T., Algebraic Reconstruction Techniques (ART) for Three-dimensional Electron Microscopy and X-ray Photography, *J. theor. Biol.*, 29, 471-481, 1970
- [16] Hapgood, M., A., *Space Physics Coordinate Transformations: A User Guide*, *Planet. Space Sci.*, Vol. 40, No. 5, 711-717, 1992
- [17] Heckbert, P. S., Hanrahan, P., Beam tracing polygonal objects, *Computer Graphics* 18(3), 119-127, 1984
- [18] Kak, A. C., Malcolm, S., *Principles of Computerized Tomographic Imaging, Classics in Applied Mathematics*, Siam, 2001
- [19] Kivelson, M., Russell, C., *Introduction to Space Physics*, Cambridge University Press, 1995
- [20] Langetepe, E., Zachmann, G., *Geometric Data Structures for Computer Graphics*, A K Peters Ltd, 2006
- [21] Likhachov, A.V., Pickalov, V.V., Chugunova, N.V., Baranov, V.A., Development of Iterative Algorithms for Industrial Tomography, 1st World Congress on Industrial Process Tomography, Buxton, Greater Manchester, April 14-17, 1999
- [22] Mueller, K., Yagel, R., Rapid 3D Cone-Beam Reconstruction with the Simultaneous Algebraic Reconstruction Technique (SART) Using 2D Texture Mapping Hardware, *IEEE transactions on Medical Imaging*, Vol. 19, No. 12, 1227, December, 2000
- [23] Natterer, F., *The Mathematics of Computerized Tomography, Classics in Applied Mathematics*, Siam, 2001

- [24] Press, W.H., Flannery, B.P, Teukolsky, S.A., Vetterling, W.T., Numerical Recipes in C: The Art of Scientific Computing, 2nd edition, Cambridge University Press, 1992
- [25] Rangayyan, R., Dhawan, A. P., Gordon, R., Algorithms for limited-view computed tomography: an annotated bibliography and a challenge, Applied Optics, Vol. 24, No. 23, 1 December, 1985
- [26] Saksena, R., Satyamurthy, P., Khanna, A., Munshi, P, Performance of tomographic reconstruction algorithms for limited view tomography, Proc. National Conference on Image Processing, Bangalore, India, 21-24, 2005
- [27] Yau, A.W., James, H.G., Liu, W., The Canadian Enhanced Polar Outflow Probe (e-POP) mission in ILWS, Adv. Sp. Res., 38(8), 1870-1877, DOI: 10.1016/j.asr.2005.01.058, 2006